Millimeter Interferometric HCN(1–0) and HCO$^+$(1–0) Observations of Luminous Infrared Galaxies

Masatoshi Imanishi[1]

National Astronomical Observatory, 2-21-1, Osawa, Mitaka, Tokyo 181-8588, Japan

masa.imanishi@nao.ac.jp

Kouichiro Nakanishi[1]

Nobeyama Radio Observatory, Minamimaki, Minamisaku, Nagano, 384-1305, Japan

Yoichi Tamura[2]

Department of Astronomy, The University of Tokyo, 7-3-1 Hongo, Bunkyo-ku, Tokyo 113-0033, Japan

Nagisa Oi

Department of Astronomy, School of Science, Graduate University for Advanced Studies, Mitaka, Tokyo 181-8588

and

Kotaro Kohno

Institute of Astronomy, University of Tokyo, 2-21-1, Osawa, Mitaka, Tokyo, 181-0015, Japan

ABSTRACT

We present the results on millimeter interferometric observations of four luminous infrared galaxies (LIRGs), Arp 220, Mrk 231, IRAS 08572+3915, and

---

[1]Department of Astronomy, School of Science, Graduate University for Advanced Studies, Mitaka, Tokyo 181-8588

[2]National Astronomical Observatory of Japan, 2-21-1 Osawa, Mitaka, Tokyo 181-8588, Japan

VV 114, and one Wolf-Rayet galaxy, He 2–10, using the Nobeyama Millimeter Array (NMA). Both the HCN(1–0) and HCO$^+$(1–0) molecular lines were observed simultaneously and their brightness-temperature ratios were derived. High-quality infrared L-band (2.8–4.1 μm) spectra were also obtained for the four LIRGs to better constrain their energy sources deeply buried in dust and molecular gas. When combined with other LIRGs we have previously observed with NMA, the final sample comprised nine LIRGs (12 LIRGs' nuclei) with available interferometric HCN(1–0) and HCO$^+$(1–0) data—sufficient to investigate the overall trend in comparison with known AGNs and starburst galaxies. We found that LIRGs with luminous buried AGN signatures at other wavelengths tend to show high HCN(1–0)/HCO$^+$(1–0) brightness-temperature ratios as seen in AGN-dominated galaxies, while the Wolf-Rayet galaxy He 2–10 displays a small ratio. An enhanced HCN abundance in the interstellar gas surrounding a strongly X-ray-emitting AGN, as predicted by some chemical calculations, is a natural explanation of our results.

Subject headings: galaxies: active — galaxies: nuclei — galaxies: ISM — radio lines: galaxies — galaxies: individual (Arp 220, Mrk 231, IRAS 08572+3915, VV 114 and He 2–10)

1. Introduction

It has recently been found that supermassive blackholes (SMBH) with masses of $M_{\rm SMBH} > 10^6 M_\odot$ are ubiquitously present at the centers of spheroidal components (bulges and elliptical galaxies) (Magorrian et al. 1998). When active mass accretion onto a SMBH occurs, it is observed as an active galactic nucleus (AGN). The current AGN picture postulates that dust is present in torus geometry around the central SMBH (Antonucci 1993). The direction perpendicular to the torus is mostly transparent to the bulk of the AGN's ionizing UV – soft X-ray photons. Gas clouds at 10–1000 pc distances from the AGN along the torus axis, photo-ionized by the central AGN's radiation, produce the so-called narrow-line regions (NLRs; Robson 1996). Since the spectral shapes of the ionizing photons differ between AGNs and stars, emission-line ratios from NLRs differ from gas clouds photo-ionized in star-forming galaxies. Thus, AGNs surrounded by torus-shaped dust with well developed NLRs are distinguishable from star-forming galaxies relatively easily (Veilleux & Osterbrock 1987).

Because dust at the central <10 pc of galaxies has an angular momentum, the spatial distribution of the dust is likely to be axisymmetrical; dust column density is higher in one direction (the torus direction) and lower in another direction (the torus axis). When the

nuclear concentration of dust becomes large, even the torus axis direction can be opaque to the bulk of the AGN's UV – soft X-ray radiation, and the radiation can be blocked at the inner part (<10 pc), producing virtually no NLRs. Such *buried* AGNs are no longer detectable as long as emission lines originating in the NLRs are sought. Because a simple interpretation of the cosmic X-ray background spectrum suggests that most AGNs in the universe are buried (Fabian & Iwasawa 1999), it is important to establish a technique for finding buried AGNs. In a buried AGN, almost all of the energetic UV – soft X-ray radiation is absorbed by the surrounding dust and is re-emitted as infrared dust emission. For this reason, *luminous* buried AGNs are expected to be strong infrared emitters. Luminous infrared galaxies (LIRGs), which radiate strong infrared emission with $L_{IR} > 10^{11} L_{\odot}$ and contain highly concentrated nuclear dust (Sanders & Mirabel 1996), are probable objects in which luminous buried AGNs reside.

Since star-forming activity can also produce infrared emission, it is necessary to distinguish the origin of the infrared luminosities of LIRGs if we are to study the luminous buried AGN population. An effective method is to search for the presence of strong X-ray emission because an AGN intrinsically produces much stronger X-ray emission compared to star-forming activity (Robson 1996). Unfortunately, buried AGNs generally contain a large amount of nuclear dust (Imanishi et al. 2006a), and most of them may be Compton-thick ($N_H > 10^{24}$ cm^{-2}) sources (Maiolino et al. 2003). X-ray observations at E > 10 keV are needed to directly detect Compton-thick X-ray emission from luminous buried AGNs with a small scattered/reflected component (Fabian et al. 2002); however, these are applicable only to a few very nearby bright LIRGs due to a current sensitivity limit.

Although a systematic buried AGN search through direct X-ray observations is difficult, we can investigate the presence of a luminous buried AGN through the chemical effects of the intrinsically strong X-ray emission on the surrounding interstellar medium. Around a strongly X-ray-emitting buried AGN surrounded by dense gas and dust, the so-called X-ray dissociation regions (XDR; Maloney et al. 1996) should develop, in contrast to photo-dissociation regions (PDRs) usually seen in strongly UV-emitting star-forming regions. Detection of XDR signatures can thus be a useful tool for locating a luminous buried AGN. Among the several proposed probes of XDRs (Usero et al. 2004; Aalto et al. 2007), we focus on the *observationally derived* method based on HCN(1–0) and HCO$^+$(1–0) line ratios (Kohno et al. 2001; Kohno 2005; Imanishi et al. 2006b; Gracia-Carpio et al. 2006), because theoretical prediction of line fluxes from PDRs and XDRs requires many free parameters (Yamada et al. 2007) and could still be uncertain, given that the most important parameter—detailed properties of the clumpy structure of molecular gas (Solomon et al. 1987)—is totally unknown from observations.

Here, we present the results of our millimeter interferometric HCN(1–0) and HCO$^+$(1–0) observations using the Nobeyama Millimeter Array (NMA) of nearby LIRGs whose energy sources have previously been investigated at other wavelengths. Compared to previous HCN(1–0) and HCO$^+$(1–0) observations of LIRGs using single-dish radio telescopes (Gao & Solomon 2004; Gracia-Carpio et al. 2006), our interferometric maps have the important advantage that spatially resolved HCN(1–0) and HCO$^+$(1–0) data are obtainable in LIRGs, which often show disturbed, multiple nuclei morphologies (Sanders & Mirabel 1996). New ground-based infrared L-band (2.8–4.1 μm) spectra of higher quality than older data were also taken for individual main nuclei of these millimeter-observed LIRGs to better constrain the nature of their obscured energy sources. We adopted H$_0$ = 75 km s^{-1} Mpc^{-1}, $\Omega_{\rm M}$ = 0.3, and Ω_Λ = 0.7 throughout this paper.

2. Targets

The target LIRGs are selected on the basis of their proximity ($z < 0.06$) to cover the redshifted HCN(1–0) and HCO$^+$(1–0) emission lines with the NMA receiving systems, and their expected high fluxes of HCN(1–0) and HCO$^+$(1–0). The four LIRGs, Arp 220, IRAS 08572+3915, Mrk 231, and VV 114, were observed. Table 1 summarizes the infrared emission properties of these LIRGs. An angular scale of $1''$ corresponds to a physical size of 0.3–1 kpc at redshift = 0.018–0.058.

Arp 220 (z = 0.018) is one of the best-studied nearby ultraluminous infrared galaxies (ULIRGs; L$_{\rm IR}$ > 10^{12}L$_\odot$; Sanders et al. 1988a). It consists of two nuclei, Arp 220 E and W, with a separation of $\sim$1$''$ (Scoville et al. 2000; Soifer et al. 2000), and the optical spectrum of the combined emission is classified as a LINER (i.e., non-Seyfert; no obvious AGN signatures in the optical spectrum) (Veilleux et al. 1999). The presence of starburst activity (= active star-formation) is evident in various observational data (Genzel et al. 1998; Imanishi & Dudley 2000), but the detected starburst is energetically insufficient to fully account for the observed infrared luminosity of Arp 220 quantitatively (Imanishi et al. 2006a; Armus et al. 2007; Imanishi et al. 2007), requiring the energy source deeply buried in Arp 220's nuclear core (Spoon et al. 2004; Gonzalez-Alfonso et al. 2004). The presence of a luminous buried AGN at the core has long been unclear even through detailed observations in the X-ray (Iwasawa et al. 2005), infrared (Genzel et al. 1998; Armus et al. 2007), and radio (Shioya et al. 2001; Parra et al. 2007) frequencies. However, the recent discovery of a compact energy source with a very high emission surface brightness has provided the first strong signatures of a luminous buried AGN in Arp 220W (Downes & Eckart 2007).

Mrk 231 (z = 0.042) is a well studied, single nucleus ULIRG and is the most luminous

object ($L_{\rm IR} \sim 10^{12.5} L_\odot$) in the local universe. It is an optically known AGN classified as a Seyfert 1 galaxy (Veilleux et al. 1999), but it displays absorption features in the infrared spectra (Roche et al. 1983; Armus et al. 2007) and X-rays (Braito et al. 2004) possibly originating in the broad absorption line (BAL) clouds (Boksenberg et al. 1977). The presence of a very luminous and probably energetically dominant AGN is revealed by various observations (e.g., Soifer et al. 2000; Imanishi & Dudley 2000; Braito et al. 2004; Imanishi et al. 2006a).

IRAS 08572+3915 (z = 0.058) is a ULIRG ($L_{\rm IR} \sim 10^{12.1} L_\odot$) consisting of two nuclei (NW and SE) with a separation of $\sim 5''$ (Scoville et al. 2000; Kim et al. 2002). The NW nucleus (IRAS 08572+3915NW) is believed to be energetically dominant (Soifer et al. 2000) and is therefore our primary interest. It is classified optically as a LINER (Veilleux et al. 1999). It is one of the strong *buried* AGN candidates because (1) the energy source is suggested to be very compact and is more centrally concentrated than the nuclear dust, as expected for a buried AGN (Dudley & Wynn-Williams 1997; Soifer et al. 2000; Imanishi et al. 2006a, 2007), and (2) the polycyclic aromatic hydrocarbons (PAH) emission (the starburst indicator) is extremely weak (Imanishi & Dudley 2000; Imanishi et al. 2006a; Spoon et al. 2006; Armus et al. 2007; Imanishi et al. 2007). It is thus a particularly interesting target for investigating whether the HCN(1–0) to HCO$^+$(1–0) brightness-temperature ratio is similar to those found in AGN-dominated nuclei or starburst-dominated galaxies (Kohno 2005).

VV 114 (z = 0.020) is a double-nuclei LIRG ($L_{\rm IR} \sim 10^{11.6} L_\odot$) with a separation of $\sim 15''$ (Knop et al. 1994). Both nuclei are classified optically as HII regions (Veilleux et al. 1995). In the short optical wavelength, the western nucleus (VV 114W) is brighter than the eastern nucleus (VV 114E), but VV 114E becomes more important with increasing wavelength and is prominent in the infrared band (Knop et al. 1994; Le Floc'h et al. 2002), probably dominating the infrared luminosity of the VV 114 merging system. The VV 114E nucleus has a secondary peak $\sim 1''.5$ southwest of the VV 114E peak (VV 114E$_{\rm SW}$; Soifer et al. 2001). The presence of a luminous buried AGN is suggested in VV 114E from the strong featureless mid-infrared 15 μm continuum emission (Le Floc'h et al. 2002).

In Kohno (2005), HCN(1–0) to HCO$^+$(1–0) brightness-temperature ratios are studied in AGNs and typical starburst galaxies such as M82. In the nuclei of LIRGs, where molecular gas is very highly concentrated (Sanders & Mirabel 1996), putative star formation could be extreme in that young, massive, hot stars are more predominant than a normal starburst. To determine if such an extreme starburst shows a different HCN(1–0)/HCO$^+$(1–0) brightness-temperature ratio from a normal starburst, a nearby well studied Wolf-Rayet galaxy, He 2–10 (z = 0.003), dominated by massive, hot Wolf-Rayet stars (Allen et al. 1976) was also studied (Table 1).

3. Observations and Data Reduction

3.1. Millimeter interferometry

Interferometric observations of HCN(1–0) ($\lambda_{\mathrm{rest}} = 3.3848$ mm and $\nu_{\mathrm{rest}} = 88.632$ GHz) and HCO$^+$(1–0) ($\lambda_{\mathrm{rest}} = 3.3637$ mm or $\nu_{\mathrm{rest}} = 89.188$ GHz) lines were undertaken with the Nobeyama Millimeter Array (NMA) and the RAINBOW interferometer at the Nobeyama Radio Observatory (NRO) between 2005 January and 2007 April. Table 2 summarizes the detailed observation log. The NMA consists of six 10-m antennas and observations were undertaken using the AB (the longest baseline was 351 m), C (163 m), and D (82 m) configurations. The RAINBOW interferometer is a seven-element combined array that includes the NRO 45-m telescope in addition to the six 10-m antennas (NMA). The RAINBOW observations were scheduled when the NMA array was set at the AB configuration and the longest baseline was 410 m. In the 3-mm wavelength range, the sensitivity of the RAINBOW interferometer is about twice better than that of the NMA array only because the total aperture size increases by a factor of four with the inclusion of the NRO 45-m telescope.

The backend was the Ultra-Wide-Band Correlator (UWBC) (Okumura et al. 2000) configured to cover 1024 MHz with 128 channels at 8-MHz resolution. The central frequency for each source (Table 2) was set to cover both the redshifted HCN(1–0) and HCO$^+$(1–0) lines simultaneously. A bandwidth of 1024 MHz corresponds to $\sim$3500 km s^{-1} at $\nu \sim 84$–89 GHz. The field of view at this frequency is $\sim$26$''$ (full-width at half-maximum; FWHM) and $\sim$77$''$ (FWHM) for the RAINBOW and the NMA array, respectively. The Hanning window function was applied to reduce side lobes in the spectra; thus, the effective resolution was widened to 16 MHz or 55 km s^{-1} at $\nu \sim 84$–89 GHz. Since the declinations of VV 114 and He 2–10 are low ($< -15°$), an observable time period (elevation $> 20°$) per each day from the NMA site is short, requiring many observing days.

The UVPROC-II package developed at NRO (Tsutsumi et al. 1997) and the AIPS package of the National Radio Astronomy Observatory were used for standard data reduction. Corrections for the antenna baselines, band-pass properties, and the time variation in the visibility amplitude and phase were applied to all of the data (Table 2). A fraction of the data with large phase scatter due to poor millimeter seeing was removed from our analysis. After clipping a small fraction of data of unusually high amplitude, the data were Fourier-transformed using a natural UV weighting. The flux calibration was made using observations of Uranus or appropriate quasars (Table 2) whose flux levels relative to Uranus or Neptune had been measured at least every month in the NMA observing seasons. A conventional CLEAN method was applied to deconvolve the synthesized beam pattern. The primary beam pattern of the NMA antenna was corrected for LIRGs with very extended

spatial structures (VV 114 and He 2–10). Table 3 summarizes the total net on-source integration times and synthesized beam patterns. Absolute positional uncertainties of the NMA/RAINBOW maps were estimated to be much less than $1''$.

3.2. Infrared 2.8–4.1 μm (L-band) spectroscopy

We conducted ground-based infrared 2.8–4.1 μm (L-band) slit spectroscopy on the main nuclei of the four LIRGs (Arp 220, Mrk 231, IRAS 08572+3915, and VV 114) to better understand the nature of their obscured energy sources based on the equivalent width of the 3.3 μm PAH emission and the optical depths of absorption features at $\lambda_{\rm rest} \sim 3.05$ μm (in the rest frame) by ice-covered dust grains and at $\lambda_{\rm rest} \sim 3.4$ μm by bare carbonaceous dust grains (Imanishi & Dudley 2000; Imanishi & Maloney 2003). A normal starburst galaxy should always show large equivalent-width PAH emission, while a pure AGN produces a PAH-free continuum (Imanishi & Dudley 2000; Imanishi et al. 2006a). For absorption features, optical depths have upper limits in a normal starburst in which stellar energy sources and dust are spatially well mixed, while they can be arbitrarily large in a buried AGN with a more centrally concentrated energy source geometry than dust (Imanishi & Maloney 2003; Imanishi et al. 2006a). For these reasons, these PAH emission and dust-absorption features can be used to distinguish the dust-obscured energy sources of LIRGs.

Ground-based infrared spectra taken with large (>4-m) telescopes are superior in spatial resolution to those obtained by space satellites with small diameters (<1 m), thus enabling us to obtain spatially resolved spectra of double nuclei with a small separation (<2 arcsec). For example, Arp 220 and VV 114E have double nuclei with separations of 1 to 1.5 arcsec, which can be resolved only with the ground-based spectra. For Mrk 231 and IRAS 08572+3915, although infrared L-band spectra taken with <4m telescopes have been published (Imanishi et al. 1998; Imanishi & Dudley 2000; Imanishi et al. 2006a), a higher-quality L-band spectrum obtained with a larger, 8-m-class telescope may be able to provide new constraints on their energy sources. We thus obtained infrared L-band spectra of Arp 220, Mrk 231, IRAS 08572+3915, and VV 114E using the Subaru 8.2-m telescope (Iye et al. 2004) atop Mauna Kea, Hawaii.

We used the IRCS infrared spectrograph (Kobayashi et al. 2000) at the Nasmyth focus of the Subaru telescope to obtain the new infrared L-band spectra of these LIRGs. Table 4 tabulates the observation log. The sky was clear during the observations. The seeing in the K-band measured in images taken before the L-band spectroscopy was $0''\!.4$–$0''\!.8$ in FWHM. A $0''\!.6$- or $0''\!.9$-wide slit and the L-grism were used with a 52-mas-pixel scale. The achievable spectral resolution is R ~ 140–200 at $\lambda \sim 3.5$ μm. When the seeing size was sufficiently

small, we basically used the $0\rlap{.}''6$ slit to search for AGN signatures at a nuclear core based on the PAH equivalent width and the strengths of dust absorption features (Imanishi & Dudley 2000; Imanishi & Maloney 2003; Imanishi et al. 2006a) with a reduced contamination from extended starburst components. However, for IRAS 08572+3915, the $0\rlap{.}''9$ slit was employed because the seeing in the K-band worsened during the observation. Thus, PAH emission from an extended ($>0\rlap{.}''6$ or $>0\rlap{.}''9$) starburst component is not covered; thus, PAH flux or luminosity is not considered in our discussion. For Arp 220, Mrk 231, and IRAS 08572+3915, nuclear PAH fluxes (or luminosities) within the central 1–2 arcsec can better be investigated from previously obtained spectra using a wider slit (Imanishi & Dudley 2000). The precipitable water was low, 1–2 mm for the 2006 July observing run, and <1 mm for the 2007 January run. We employed a standard telescope nodding technique (ABBA pattern) with a throw of 5 to 7 arcsec along the slit to subtract background emission. We used the optical guider of the Subaru telescope to monitor the telescope tracking. Exposure time was 1.0–1.5 sec, and 30–60 coadds were made at each nod position.

For both observing runs, F- or G-type main sequence stars (Table 4) were observed as standard stars, with a mean airmass difference of <0.1 to the individual LIRG nuclei to correct for the transmission of Earth's atmosphere and to provide flux calibration. The L-band magnitudes of the standard stars were estimated from their V-band ($\lambda = 0.6~\mu$m) magnitudes, adopting the $V - L$ colors appropriate to the stellar types of individual standard stars (Tokunaga 2000).

Standard data analysis procedures were employed using IRAF [1]. Initially, frames taken with an A (or B) beam were subtracted from frames subsequently taken with a B (or A) beam, and the resulting subtracted frames were added and divided by a spectroscopic flat image. Bad pixels and pixels hit by cosmic rays were then replaced with the interpolated values of the surrounding pixels. Finally, the spectra of the LIRGs' nuclei and standard stars were extracted by integrating signals over $0\rlap{.}''8$–$1\rlap{.}''8$, depending on the actual signal profiles. To create a combined spectrum of Arp 220E+W, we summed signals over $2\rlap{.}''5$–$2\rlap{.}''9$ along the slit. Wavelength calibration was performed based on the wavelength-dependent transmission of Earth's atmosphere. The spectra of the LIRGs' nuclei were divided by the observed spectra of standard stars and multiplied by the spectra of blackbodies with temperatures appropriate to individual standard stars (Table 4).

Flux calibration was performed based on signals of the LIRGs and standard stars de-

---

[1]IRAF is distributed by the National Optical Astronomy Observatories, which are operated by the Association of Universities for Research in Astronomy, Inc. (AURA), under cooperative agreement with the National Science Foundation.

tected inside our slit spectra. Seeing sizes in the K-band (and L-band) were always smaller than the employed slit widths, and good telescope tracking performance of Subaru was established. We thus expected possible slit loss for the compact ($<0\rlap.''6$) emission to be minimal, say $<30\%$. In fact, we divided the whole data set into subgroups and compared their flux levels, which agreed within 20% for all LIRGs. This level of possible flux uncertainty ($<30\%$) for the compact emission will not seriously affect our main conclusions. To reduce scatter of the infrared spectra, appropriate binning of spectral elements was performed, particularly at $\lambda_{\mathrm{obs}} < 3.3$ μm in the observed frame, where the scatter of data points is larger due to poorer Earth atmospheric transmission than at $\lambda_{\mathrm{obs}} > 3.4$ μm.

4. Results

4.1. Millimeter interferometric data

For Arp 220 and Mrk 231, millimeter spectra at HCN(1–0) or HCO^{+}(1–0) emission peak positions show that the flux levels between these lines are substantially above the zero level, indicating that continuum emission is clearly present. We combined data points that are unaffected by these lines and made interferometric maps of the continuum emission. Figure 1 presents the contours of the continuum emission. The continuum emission is clearly ($>9\sigma$) detected in Arp 220 and Mrk 231. We barely see the continuum emission signature for VV 114, IRAS 08572+3915, and He 2–10, but its detection significance is $<3\sigma$. Table 5 presents the estimated continuum levels.

Figure 2 shows the integrated intensity maps of the HCN(1–0) and HCO^{+}(1–0) emission of the five observed sources (Arp 220, Mrk 231, IRAS 08572+3915, VV 114, and He 2–10). The continuum emission is subtracted for Arp 220, Mrk 231, and VV 114, but not for IRAS 08572+3915 and He 2–10 because of possible large ambiguities.

Since molecular gas is highly concentrated at the nuclei of LIRGs, the importance of high-density molecular gas ($n_{\mathrm{H}} > 10^4$ cm^{-3}) is expected to increase there (Gao & Solomon 2004). Such molecular gas is better probed with HCN(1–0) and HCO^{+}(1–0) rather than the widely used CO(1–0) because the dipole moments of HCN and HCO^{+} ($\mu > 3$ debye) are much larger than CO ($\mu \sim 0.1$ debye; Botschwina et al. 1993; Millar et al. 1997). Hence, the maps in Figure 2 reflect the spatial distribution of this important dense molecular gas. A spatially unresolved emission peak is clearly seen for Mrk 231 at the nuclear position. For IRAS 08572+3915, the spatially unresolved HCN(1–0) emission peaks at the energetically dominant NW nucleus, as expected (see § 2, paragraph 4). For He 2–10, HCO^{+}(1–0) emission displaying no significant spatial extent is found close to the CO(1–0) peak (Kobulnicky et al.

1995). A spatially extended emission component is detected for Arp 220 and VV 114. Figures 3 and 4 display the channel maps around the HCN(1–0) and HCO$^+$(1–0) lines of Arp 220 and VV 114, respectively.

For Arp 220, the HCN(1–0) and HCO$^+$(1–0) emission peaks reside in between the double nuclei in the integrated intensity maps of Figure 2. Nevertheless, the channel map in Figure 3 clearly shows that Arp 220E becomes more prominent with increasing velocity (upper-left, red component) and Arp 220W does with decreasing velocity (lower-right, blue component). Our HCN(1–0) and HCO$^+$(1–0) channel maps thus confirm that the Arp 220E nucleus is farther redshifted than Arp 220W, as was previously noted (Larkin et al. 1995; Downes & Solomon 1998; Taniguchi & Shioya 1998; Sakamoto et al. 1999).

In the case of VV 114, the HCN(1–0) the emission peak is close to VV 114E, while that of HCO$^+$(1–0) is strong between the VV 114E and W nuclei (Figure 2), similar to CO(1–0), (2–1), and (3–2) emission (Yun et al. 1994; Iono et al. 2004). The spatial distributions of HCN(1–0) and HCO$^+$(1–0) are quite different, possibly because (a) HCN(1-0) and HCO$^+$(1–0) probe molecular gas with different density (Greve et al. 2006), due to their slightly different critical densities [2], or (b) HCO$^+$ (1–0) may selectively trace shock regions, due to enhanced HCO$^+$ abundance by shocks (Dickinson et al. 1980). Further details will be discussed in a future paper (Tamura et al., in preparation). No significant HCN(1–0) or HCO$^+$(1–0) emission is recognizable in VV 114W.

Figure 5 shows spectra around the HCN(1–0) and HCO$^+$(1–0) lines for Arp 220, Mrk 231, IRAS 08572+3915, and VV 114. For Mrk 231 and IRAS 08572+3915, spectra are extracted at the nuclear peak position. For Arp 220, the spectra are extracted at both the Arp 220E and W positions, and double-peaked HCN(1–0) and HCO$^+$(1–0) emission is seen at both positions. Although the double-peaked profile suggests that emission from Arp 220E and W are not clearly spatially resolved in a map, the redshifted (lower frequency) component is stronger at the Arp 220E position than at Arp 220W, as expected from the channel map (Figure 3). We can thus separate the emission from Arp 220E and W spectroscopically, with the red and blue components coming from Arp 220E and W, respectively. For VV 114, both the HCN(1–0) and HCO$^+$(1–0) emission have spatial structures, and their peak positions

---

[2] The critical density (n_c) is, by definition, proportional to Einstein's A coefficient (A) divided by the collision rates (Schoier et al. 2005). The A-coefficient A is $\propto \mu^2 \times \nu^3$, where μ is the dipole moment and ν is the frequency of the molecular line. The dipole moments (μ) of HCN ($\mu \sim 3$ debye; Millar et al. 1997) and HCO$^+$ ($\mu \sim 4$ debye; Botschwina et al. 1993) are similar to each other. The frequencies of HCN(1–0) (88.632 GHz) and HCO$^+$(1–0) (89.188 GHz) are almost identical. Thus, the A-coefficient is similar between HCN(1–0) and HCO$^+$(1–0). However, using the collision rates estimated by Schoier et al. (2005), the n_c value of HCN(1–0) is a factor of ~ 5 larger than that of HCO$^+$(1–0).

are not the same. We thus extract spectra at four different positions: (E-1) the HCN(1–0) peak at the eastern side of VV 114E in Figure 2; (E-2) the HCN(1–0) peak at the western side of VV 114E in Figure 2; (3) the eastern HCO^+(1–0) peak between VV 114E and W in Figure 2; and (4) the western HCO^+(1–0) peak between VV 114E and W in Figure 2.

Figure 6 presents Gaussian fits to the detected HCN(1–0) and HCO^+(1–0) lines. The central velocity and line width of the Gaussian fit are determined independently for the HCN(1–0) and HCO^+(1–0) lines. For IRAS 08572+3915, a double Gaussian fit was attempted because the lines seem to be double-peaked. Table 6 summarizes the Gaussian fitting results. For Mrk 231 and IRAS 08572+3915 (the LIRGs dominated by the single primary nucleus), the HCN(1–0) peak velocity is similar to that of CO(1–0) in previous reports (Downes & Solomon 1998; Bryant & Scoville 1996; Evans et al. 2002). For Arp 220E and W nuclei, the peak velocities of HCN(1–0) and HCO^+(1–0) agree with that of CO(2–1) within 50 km s^{-1} (Downes & Solomon 1998).

For Arp 220, Mrk 231, IRAS 08572+3915, and VV 114, the integrated fluxes of HCN(1–0) and HCO^+(1–0) at each peak position estimated from the Gaussian fits in the spectra are summarized in Table 7. For He 2–10, the fluxes are derived from the peak contours of the integrated intensity maps (Figure 2) because the spectrum is noisy. The HCN(1–0)/HCO^+(1–0) brightness-temperature ratios ($\propto \lambda^2 \times$ flux density) are also shown in Table 7. In Mrk 231 and IRAS 08572+3915, both the HCN(1–0) and HCO^+(1–0) emission show a spatially unresolved single peak at the main nuclear position. The integrated HCN(1–0) and HCO^+(1–0) fluxes are also estimated from the peak contours of the integrated intensity maps in Figure 2. The estimated values are consistent with those based on the Gaussian fits for both HCN(1–0) and HCO^+(1–0) emission within 15% in Mrk 231 and 30% in IRAS 08572+3915 if the continuum in Figure 6 is assumed.

Arp 220, VV 114, and He 2–10 display spatially extended HCN(1–0) and HCO^+(1–0) emission. Their total fluxes are shown in Table 8. For Arp 220 and Mrk 231, HCN(1–0) and HCO^+(1–0) fluxes have previously been measured using single-dish radio telescopes. Table 9 compares their fluxes with our measurements, which are similar, suggesting that our interferometric data recover the bulk of HCN(1–0) and HCO^+(1–0) emission.

4.2. Infrared spectra

4.2.1. PAH emission

Figure 7 presents the flux-calibrated infrared 2.8–4.1 μm (*L*-band) spectra of Arp 220, Mrk 231, IRAS 08572+3915NW, and VV 114E. For Arp 220 and VV 114E, our ground-based

spectra provide spatially resolved spectra of double nuclei with small (1–2 arcsec) separation, which is not possible for space-based infrared spectra (see §3.2). Thus, our L-band spectra make it possible to discuss the energy sources of individual nuclei separately for Arp 220E and W (Scoville et al. 2000; Soifer et al. 2000), and VV 114E and E_{SW} (Soifer et al. 2001).

The 3.3 μm PAH emission is clearly seen in the spectra of the observed LIRGs, except for IRAS 08572+3915NW, indicating that a detectable amount of starburst activity is surely present. Table 10 summarizes the strength of the 3.3 μm PAH emission feature. The observed 3.3 μm PAH luminosities ($L_{3.3PAH}$) roughly trace the absolute magnitudes of modestly obscured ($A_V < 15$ mag) starburst activities covered inside our slit spectra (the L_{IR} of such a starburst is $\sim 10^3 \times L_{3.3PAH}$; Mouri et al. 1990; Imanishi 2002).

For Arp 220E+W, Mrk 231, and IRAS 08572+3915NW, the equivalent widths of the 3.3 μm PAH emission ($EW_{3.3PAH}$) are similar to previous estimates based on old, lower-quality spectra (Imanishi & Dudley 2000; Imanishi et al. 2006a). The $EW_{3.3PAH}$ values of Mrk 231, IRAS 08572+3915NW, and VV 114E are more than a factor of ~ 5 smaller than the typical value found in starburst-dominated galaxies ($EW_{3.3PAH} \sim 100$ nm; Imanishi & Dudley 2000), indicating that PAH-free continua from the putative luminous AGNs contribute importantly to their observed L-band fluxes (Imanishi & Dudley 2000; Imanishi et al. 2006a; Imanishi 2006). For Arp 220E, W, and VV 114E_{SW}, the $EW_{3.3PAH}$ values are as large as seen in normal starburst galaxies, so that no explicit signs of PAH-free continua from buried AGNs are detected in this wavelength range.

For Mrk 231 and IRAS 08572+3915, the ULIRGs dominated by compact nuclear emission, the L-band continuum flux levels in our slit spectra are similar, within 0.1 mag, to the photometric measurements using a 2$\farcs$5 aperture (Zhou et al. 1993). For Arp 220E+W, the L-band continuum flux level is a factor of ~ 2 smaller than previously obtained spectra using a 1$\farcs$2 aperture (Imanishi & Dudley 2000) and photometric data using a 2$\farcs$5 aperture (Zhou et al. 1993). The small flux is possibly due to the small slit width (0$\farcs$6) in the new spectra and/or possible L-band flux ambiguity in the adopted standard star, HR 5728 (Table 4).

4.2.2. Absorption features

IRAS 08572+3915NW (Figure 7) shows a strong absorption feature at $\lambda_{obs} = 3.6$ μm in the observed frame or $\lambda_{rest} = 3.4$ μm in the rest frame due to bare carbonaceous dust grains. Its optical depth is estimated to be $\tau_{3.4} \sim 0.8$, which is similar to previous estimates (Imanishi & Dudley 2000; Imanishi et al. 2006a). The optical depth is larger than the upper

limit produced with the natural geometry of a normal starburst (stellar energy sources and dust spatially well mixed; $\tau_{3.4} < 0.2$), but requires buried AGN-type geometry in which the energy source is more centrally concentrated than the dust (Imanishi & Maloney 2003; Imanishi et al. 2006a), supporting the buried-AGN classification as previously indicated from the low $EW_{3.3PAH}$ value (<3 nm; Table 10).

In the high-quality IRAS 08572+3915NW spectrum in Figure 7, the broad absorption feature centered at $\lambda_{\rm obs} = 3.2$ μm or $\lambda_{\rm rest} = 3.0$–3.05 μm is seen for the first time. In a buried AGN and starburst composite galaxy, the buried AGN emission is more highly obscured, because the central compact buried AGN should be geometrically surrounded by the starburst. Hence, the contribution from buried AGN emission to an observed flux becomes higher with increasing wavelength, from the K-band (2–2.5 μm) to L-band (2.8–4.1 μm), due to smaller dust extinction. Additionally, blackbody radiation from stars (T > 4000K) generally shows a steeply decreasing flux from the K- to L-band. For these reasons, it could happen that an observed K-band continuum emission largely comes from foreground stellar emission, in addition to buried AGN emission, while an L-band continuum, particularly at a longer wavelength part, is dominated by buried AGN emission. If this is the case for IRAS 08572+3915NW and if the stellar emission's tail extends from the K-band to the shorter part of the L-band ($\lambda_{\rm obs} < 3.0$ μm), then an absorption-like feature at $\lambda_{\rm rest} \sim$ 3.05 μm could be reproduced. However, the K-band spectrum of IRAS 08572+3915 comes mostly from buried-AGN-heated hot dust emission, because of the extremely red K-band continuum and no stellar CO absorption features at $\lambda_{\rm rest} \sim 2.3$ μm (Goldader et al. 1995; Imanishi et al. 2006a). Thus, this scenario seems implausible. We ascribe the absorption-like feature to the 3.05 μm absorption by ice-covered dust grains and estimate its optical depth to be $\tau_{3.1} \sim 0.3$.

The spectrum of VV 114E also displays the 3.05 μm ice-absorption feature with an optical depth of $\tau_{3.1} \sim 0.5$. Its optical depth is again larger than the threshold explained by the mixed dust/source geometry of a normal starburst ($\tau_{3.1} < 0.3$; Imanishi & Maloney 2003), suggesting the presence of a luminous buried AGN, as inferred from the low $EW_{3.3PAH}$ value ($\sim$20 nm; Table 10).

For the infrared L-band spectra of the remaining LIRG nuclei (Arp 220E, W, Mrk 231, and VV 114E$_{\rm SW}$), no clear absorption features are recognizable. The absence of absorption features in Mrk 231 (the low $EW_{3.3PAH}$ object; Table 10) implies that the AGN is only weakly obscured, while those for Arp 220E, W, and VV 114E$_{\rm SW}$ are explained by the predominant contribution from starburst emission to the observed L-band fluxes. For Arp 220W, the nucleus with luminous buried AGN signatures (Downes & Eckart 2007), we see no explicit AGN sign in the infrared L-band spectrum. The emission from the putative buried AGN

may be so highly flux-attenuated that its contribution to an observed L-band flux must be insignificant, compared to foreground weakly-obscured starburst emission.

5. Discussion

5.1. Comparison of HCN(1–0)/HCO$^+$(1–0) brightness-temperature ratios with other galaxies

Figure 8 shows the HCN(1–0)/HCO$^+$(1–0) and HCN(1–0)/CO(1–0) brightness-temperature ratios for Arp 220, Mrk 231, IRAS 08572+3915, VV 114, and He 2–10. Previously obtained data points of nearby LIRGs (Imanishi et al. 2004, 2006b; Imanishi & Nakanishi 2006), starbursts, and Seyfert galaxies (Kohno 2005) are also plotted. As stated by Imanishi et al. (2006b), we mainly use the HCN(1–0)/HCO$^+$(1–0) ratios (ordinate) in our discussions for the following reasons. First, since the HCN(1–0) and HCO$^+$(1–0) lines are observed simultaneously with the same array configuration of NMA/RAINBOW, their beam patterns are virtually identical. We can thus be confident that the same regions are probed with both lines. Second, both HCN(1–0) and HCO$^+$(1–0) fluxes are measured at the same time with the same receiver and same correlator unit so that the possible *absolute* flux calibration uncertainty of interferometric data does not propagate to the uncertainty in the ratio, which is dominated by statistical noise and fitting errors (see Figure 6). Therefore, the derivation of the HCN(1–0)/HCO$^+$(1–0) brightness-temperature ratio is straightforward. Neither of the first and second arguments hold for the HCN(1–0)/CO(1–0) brightness-temperature ratios in the abscissa of Figure 8, which complicates their interpretation. LIRGs with luminous AGN signatures at other wavelengths (Arp 220W, Mrk 231, IRAS 08572+3915) tend to show high HCN(1–0)/HCO$^+$(1–0) brightness-temperature ratios as seen in AGN-dominated galaxies. The ratio is also high in VV 114E-1, which is close to the putative AGN location at VV 114E, despite a slight positional deviation. The Wolf-Rayet galaxy He 2–10 shows a very low HCN(1–0)/HCO$^+$(1–0) brightness-temperature ratio. Some individual examples of the nearby Galactic high-mass-star-forming, HII-region cores show high HCN(1–0)/HCO$^+$(1–0) brightness-temperature ratios (Turner & Thaddeus 1977; Pirogov 1999). However, for external galaxies, the ensemble of HII regions, molecular gas, and PDRs will be observed as a whole. The low HCN(1–0)/HCO$^+$(1–0) brightness-temperature ratio in He 2–10 suggests that even an extreme starburst dominated by young hot stars cannot easily produce a high HCN(1–0)/HCO$^+$(1–0) brightness-temperature ratio when observed at a large physical scale. The high ratios observed in LIRGs are likely to have another cause than the extreme starburst scenario.

5.2. Interpretations of HCN(1–0)/HCO$^+$(1–0) brightness-temperature ratios

A natural explanation for the high HCN(1–0)/HCO$^+$(1–0) brightness-temperature ratios in buried AGN candidates is the increasing abundance of HCN due to strong X-ray radiation from the AGN, as predicted by some simple chemical calculations (Lepp & Dalgarno 1996; Lintott & Viti 2006). When both the HCN(1–0) and HCO$^+$(1–0) emission are optically thin, the HCN(1–0)/HCO$^+$(1–0) brightness-temperature ratio will increase linearly with increasing HCN abundance relative to HCO$^+$. Imanishi et al. (2006b) and Figure 9 show that even if the emission is moderately optically thick, the increasing HCN abundance results in a larger HCN(1–0)/HCO$^+$(1–0) brightness-temperature ratio (see also Knudsen et al. 2007). Since the HCN(1–0)/HCO$^+$(1–0) brightness-temperature ratios in Figure 8 derived from our NMA/RAINBOW data are only toward the cores where putative AGNs are expected to be present, with a minimum contamination from extended starburst emission outside the beam size, the potential AGN's X-ray chemistry, if any, may better be reflected than single-dish telescope's measurements.

The critical density (n_c) HCN(1–0) is a factor of $\sim$5 larger than that of HCO$^+$(1–0) (§ 4.1). When the fraction of high density gas, above the HCN(1–0) critical density, increases, the HCN(1–0)/HCO$^+$(1–0) brightness-temperature ratio could be high compared to low density gas. Since LIRGs have highly concentrated molecular gas in their nuclei (Sanders & Mirabel 1996) and the density may be larger than the normal starburst galaxies studied by Kohno (2005), the large HCN(1–0)/HCO$^+$(1–0) brightness-temperature ratios could originate simply in the increased molecular gas density. However, in this scenario, the HCN(1–0)/CO(1–0) brightness-temperature ratios should be correspondingly high (see §4.1). Although HCN(1–0)/CO(1–0) brightness-temperature ratios in the abscissa of Figure 8 exhibit some ambiguities (§ 5.1), no such expected trend is observed in Figure 8 (LIRGs are not distributed in the right side), which does not support this high gas-density scenario. The expected high gas density in the nuclei of LIRGs and non-high HCN(1–0)/CO(1–0) brightness-temperature ratios can be reconciled if the higher average gas density in certain areas results from a larger volume-filling factor of the clump (Figure 9), rather than the higher density of each clump.

Garcia-Burillo et al. (2006) found a very large HCN(5–4)/HCO$^+$(5–4) brightness-temperature ratio in a luminous AGN with strong mid-infrared 12 μm continuum emission (APM 08279+5255), and suggested that infrared radiative pumping, rather than collisional excitation, can produce a high HCN/HCO$^+$ brightness-temperature ratio. In general, an AGN is a more luminous mid-infrared 12 μm continuum emitter than a starburst, because 12 μm hot dust emission is stronger in the former. Hence, the infrared pumping may work more effectively in LIRGs with luminous buried AGNs than those without, which could also explain the high HCN(1–

0)/HCO$^+$(1–0) brightness-temperature ratios seen in luminous buried AGN candidates.

Papadopoulos (2007) proposed that the HCN(1–0)/HCO$^+$(1–0) brightness-temperature ratio could increase with increasing turbulence of molecular gas. In this model, it is expected that the ratio is higher with larger line widths of HCN(1–0) and HCO$^+$(1–0). Figure 10 compares the line width with the ratio, but we see no clear positive trend.

Gracia-Carpio et al. (2006) measured the HCN(1–0) and HCO$^+$(1–0) fluxes of LIRGs using a single-dish telescope with >25-arcsec beam size, and found a positive correlation between the HCN(1–0)/HCO$^+$(1–0) brightness-temperature ratio and infrared luminosity. Figure 11 shows the HCN(1–0)/HCO$^+$(1–0) brightness-temperature ratio only for the *core* emission inside 1.5–10 arcsec beam sizes as a function of infrared luminosity from the whole galactic region. Among LIRGs plotted in Figure 11, the two LIRGs dominated by a single main nucleus, Mrk 231 and Mrk 273, were plotted in the figure of Gracia-Carpio et al. (2006). The two LIRGs with multiple main nuclei, Arp 220 and Arp 299, were also studied by Gracia-Carpio et al. (2006), but our interferometric data resolved the nuclei, providing essentially new plots. Other LIRGs in Figure 11 are new. A positive correlation is also recognizable here with a different sample. If our AGN's X-ray interpretation for the origin of high HCN(1–0)/HCO$^+$(1–0) brightness-temperature ratios is correct, then an increasing importance of AGNs at the cores of LIRGs with higher infrared luminosities is suggested. Investigating the spatial variation of the ratios using a better spatial-resolution map (i.e., separating a true compact core and surrounding extended regions) may help to clarify the origin of the ratios. Detailed theoretical calculations that solve chemical reaction networks in a self-consistent way and realistically account for the clumpy structure of molecular gas are also desirable for interpreting our observational results.

6. Summary

We presented the results of millimeter interferometric HCN(1–0) and HCO$^+$(1–0) observations of nearby LIRGs using the NMA/RAINBOW array. When combined with other LIRGs we have previously observed, ours is the largest interferometric HCN(1–0) and HCO$^+$(1–0) survey of LIRGs. Most of the observed LIRGs are selected based on the presence of luminous AGN signatures at other wavelengths. From the interferometric data, we extracted the HCN(1–0) and HCO$^+$(1–0) flux at the core positions, where the putative AGNs are expected to be present. For observationally investigating the possible chemical effects of the putative strongly X-ray-emitting AGN to the surrounding interstellar gas, our data set is much more advantageous than single-dish telescope's data because the contamination from extended starburst emission can be reduced. We derived the HCN(1–0)/HCO$^+$(1–0)

brightness-temperature ratios of LIRGs and compared them to the ratios found in AGNs and starburst galaxies.

We reached the following main conclusions.

1. LIRGs with detected luminous AGN signatures through observations at other wavelengths generally show high $HCN(1–0)/HCO^+(1–0)$ brightness-temperature ratios and are distributed in the region occupied by AGNs.

2. When combined with $HCN(1–0)/CO(1–0)$ brightness-temperature ratios and the line widths of $HCN(1–0)$ and $HCO^+(1–0)$, the high $HCN(1–0)/HCO^+(1–0)$ brightness-temperature ratios observed in these LIRGs are naturally explained by an HCN abundance enhancement as suggested by some simple theoretical models.

3. We found a positive correlation between the $HCN(1–0)/HCO^+(1–0)$ brightness-temperature ratios only toward the LIRGs' cores and infrared luminosities of LIRGs, suggesting that AGN activity is more important in galaxies with higher infrared luminosities.

REFERENCES

Aalto, S., Spaans, M., Wiedner, M. C., & Huttemeister, S. 2007, A&A, 464, 193

Allen, D. A., Wright, A. E., & Goss, W. M. 1976, MNRAS, 177, 91

Antonucci, R. 1993, ARA&A, 31, 473

Armus, L., et al. 2007, ApJ, 656, 148

Boksenberg, A., Carswell, R. F., Allen, D. A., Fosbury, R. A. E., Penston, M. V., & Sargent, W. L. W. 1977, MNRAS, 178, 451

Botschwina, P., Horn, M., Flugge, J., Seeger, S. 1993, J. Chem. Soc. Faraday Trans., 89, 2219

Braito, V. et al. 2004, A&A, 420, 79

Bryant, P. M., & Scoville, N. Z. 1996, ApJ, 457, 678

Charmandaris, V., Stacey, G. J., & Gull, G., 2002, ApJ, 57

Condon, J. J., Huang, Z.-P., Yin, Q. F., & Thuan, T. X. 1991, ApJ, 378, 65

Dickinson, D. F., Rodriguez Kuiper, E. N., St. Clair Dinger, A., & Kuiper, T. B. H. 1980, ApJ, 237, L43

Downes, D., & Eckart, A. 2007, A&A, L57

Downes, D., & Solomon, P. M. 1998, ApJ, 507, 615

Dudley, C. C., & Wynn-Williams, C. G. 1997, ApJ, 488, 720

Evans, A. S., Mazzarella, J. M., Surace, J. A., & Sanders, D. B. 2002, ApJ, 580, 749

Evans, A. S., Solomon, P. M., Tacconi, L. J., Vavilkin, T., & Downes, D. 2006, AJ, 132, 2398

Fabian, A. C., & Iwasawa, K. 1999, MNRAS, 303, L34

Fabian, A. C., Wilman, R. J., & Crawford, C. S., 2002, MNRAS, 329, L18

Gao, Y., & Solomon, P. M. 2004, ApJS, 152, 63

Garcia-Burillo, S., et al. 2006, ApJ, 645, L17

Genzel, R. et al. 1998, ApJ, 498, 579

Gierens, K. M., Stutzki, J., & Winnewisser, G. 1992, A&A, 259, 271

Goldader, J. D., Joseph, R. D., Doyon, R., & Sanders, D. B. 1995, ApJ, 444, 97

Gonzalez-Alfonso, E., Smith, H. A., Fischer, J., & Cernicharo, J., 2004, ApJ, 613, 247

Gracia-Carpio, J., Garcia-Burillo, S, Planesas, P., & Colina, L. 2006, ApJ, 640, L135

Greve, T. R., Papadopoulos, P. P., Gao, Y., & Radford, S. J. E. 2006, astro-ph/0610378

Imanishi, M. 2002, ApJ, 569, 44

Imanishi, M., 2006, AJ, 131, 2406

Imanishi, M., & Dudley, C. C. 2000, ApJ, 545, 701

Imanishi, M., Dudley, C. C., & Maloney, P. R. 2006a, ApJ, 637, 114

Imanishi, M., Dudley, C. C., Maiolino, R., Maloney, P. R., Nakagawa, T., & Risaliti, G. 2007, ApJS, 171, 72

Imanishi, M., & Maloney, P. R. 2003, ApJ, 588, 165

Imanishi, M., & Nakanishi, K. 2006, PASJ, 58, 813

Imanishi, M., Nakanishi, K., Kuno, N., & Kohno, K. 2004, AJ, 128, 2037

Imanishi, M., Nakanishi, K., & Kohno, K. 2006b, AJ, 131, 2888

Imanishi, M., Terada, H., Goto, M., & Maihara, T. 1998, PASJ, 50, 399

Iono, D., Ho, P. T. P., Yun, M. S., Matsushita, S., Peck, A. B., & Sakamoto, K. 2004, ApJ, 616, L63

Iwasawa, K., Sanders, D. B., Evans, A. S., Trentham, N., Miniutti, G., & Spoon, H. W. W. 2005, MNRAS, 357, 565

Iye, M. et al., 2004, PASJ, 56, 381

Kim, D. -C., Veilleux, S., & Sanders, D. B., 2002, ApJS, 143, 277

Knop, R. A., Soifer, B. T., Graham, J. R., Matthews, K., Sanders, D. B., & Scoville, N. Z. 1994, AJ, 107, 920

Knudsen, K. K., Walter, F., Weiss, A., Bolatto, A., Riechers, D. A., & Menten, K. 2007, ApJ, 666, 156

Kobayashi, N., et al. 2000, IRCS: Infrared camera and spectrograph for the Subaru Telescope, in Proc. SPIE 4008: Optical and IR Telescope Instrumentation and Detectors, eds M. Iye & A. F. Moorwood, 1056

Kobulnicky, H. A., Dickey, J. M., Sargent, A. I., Hogg, D. E., & Conti, P. S. 1995, AJ, 110, 116

Kohno, K. 2005, in AIP Conf. Ser. 783, The Evolution of Starbursts, ed. S. Hüttemeister, E. Manthey, D. Bomans, & K. Weis (New York: AIP), 203 (astro-ph/0508420)

Kohno, K., Matsushita, S., Vila-Vilaro, B., Okumura, S. K., Shibatsuka, T., Okiura, M., Ishizuki, S., Kawabe, R. 2001, in ASP Conf. Ser. 249, The Central kpc of Starbursts and AGN, ed. J. H. Knapen, J. E., Beckman, I. Shlosman, & T. J. Mahoney (San Francisco: ASP), 672 (astro-ph/0206398)

Larkin, J. E., Armus, L., Knop, R. A., Matthews, K., & Soifer, B. T. 1995, ApJ, 452, 599

Le Floc'h, E., Charmandaris, V., Laurent, O., Mirabel, I. F., Gallais, P., Sauvage, M., Vigroux, L., & Cesarsky, C. 2002, A&A, 391, 417

Lepp, S., & Dalgarno, A. 1996, A&A, 306, L21

Lintott, C., & Viti, S. 2006, ApJ, 646, L37

Magorrian, J. et al. 1998, AJ, 115, 2285

Maiolino, R. et al. 2003, MNRAS, 344, L59

Maloney, P., Hollenbach, D., & Tielens, A. G. G. M. 1996, ApJ, 466, 561

Millar, T. J., Farquhar, P. R. A., & Willacy, K. 1997, A&AS, 121, 139

Mouri, H., Kawara, K., Taniguchi, Y., & Nishida, M. 1990, ApJ, 356, L39

Nguyen-Q-Rieu, Jackson, J. M., Henkel, C., Truong-Bach, & Mauersberger, R. 1992, ApJ, 399, 521

Okumura, S. et al. 2000, PASJ, 52, 393

Papadopoulos, P. P. 2007, ApJ, 656, 792

Parra, R., Conway, J. E., Diamond, P. J., Thrall, H., Lonsdale, C. J., Lonsdale, C. J., Smith, H. E. 2007, ApJ, 659, 314

Pirogov, L. 1999, A&A, 348, 600

Radford, S. J. E., et al. 1991, in IAU Symp. 146, Dynamics of Galaxies and Their Molecular Cloud Distributions, ed. F. Combes & F. Casoli (Dordrecht: Kluwer), 303

Riechers, D. A. et al. 2006, ApJ, 650, 604

Robson, I. 1996, Active Galactic Nuclei (New York: Wiley)

Roche, P. F., Aitken, D. K., & Whitmore, B. 1983, MNRAS, 205, 21p

Sakamoto, K., Scoville, N. Z., Yun, M. S., Crosas, M., Genzel, R., & Tacconi, L. J. 1999, ApJ, 514, 68

Sanders, D. B., & Mirabel, I. F. 1996, ARA&A, 34, 749

Sanders, D. B., Soifer, B. T., Elias, J. H., Madore, B. F., Matthews, K., Neugebauer, G., & Scoville, N. Z. 1988a, ApJ, 325, 74

Sanders, D. B., Soifer, B. T., Elias, J. H., Neugebauer, G., & Matthews, K. 1988b, ApJ, 328, L35

Schoier, F. L., van der Tak, F. F. S., van Dishoeck, E. F., & Black, J. H. 2005, A&A, 432, 369

Scoville, N. Z. et al. 2000, AJ, 119, 991

Shioya, Y., Trentham, N., & Taniguchi, Y. 2001, ApJ, 538, L29

Soifer, B. T. et al. 2000, AJ, 119, 509

Soifer, B. T. et al. 2001, AJ, 122, 1213

Solomon, P. M., Downes, D., & Radford, S. J. E. 1992, ApJ, 387, L55

Solomon, P. M., Rivolo, A. R., Barrett, J., & Yahil, A. 1987, ApJ, 319, 730

Spoon, H. W. W., Moorwood, A. F. M., Lutz, D., Tielens, A. G. G. M., Siebenmorgen, R., & Keane, J. V. 2004, A&A, 414, 873

Spoon, H. W. W., Tielens, A. G. G. M., Armus, L., Sloan, G. C., Sargent, B., Cami, J., Charmandaris, V., & Houck, J. R. 2006, ApJ, 638, 759

Taniguchi, Y., & Shioya, Y. 1998, ApJ, 501, L167

Tokunaga, A. T. 2000, in Allen's Astrophysical Quantities, ed. A. N. Cox (4th ed; Berlin: Springer), 143

Tsutsumi, T. Morita, K. -I. & Umeyama, S. 1997, in Astronomical Data Analysis Software and Systems VI, ed. G. Hunt, & H. E. Payne (San Francisco: ASP), 50

Tully, R. B. 1988, Nearby Galaxies Catalog (Cambridge: Cambridge Univ. Press)

Turner, B. E., & Thaddeus, P. 1977, ApJ, 211, 755

Usero, A., Garcia-Burillo, S., Fuente, A., Martin-Pintado, J., Rodriguez-Fernandez, N. J. 2004, A&A, 419, 897

Veilleux, S., & Osterbrock, D. E. 1987, ApJS, 63, 295

Veilleux, S., Kim, D. -C., Sanders, D. B., Mazzarella, J. M., & Soifer, B. T. 1995, ApJS, 98, 171

Veilleux, S., Kim, D. -C., & Sanders, D. B. 1999, ApJ, 522, 113

Yamada, M., Wada, K., & Tomisaka, K. 2007, ApJ, in press (arXiv/0708.1045)

Yun, M. S., Scoville, N. Z., & Knop, R. A. 1994, ApJ, 430, L109

Zhou, S., Wynn-Williams, C. G., & Sanders, D. B. 1993, ApJ, 409, 149

Table 1.   Detailed information about the observed LIRGs and the Wolf-Rayet galaxy He 2–10

Object (1)	Redshift (2)	f_{12} (Jy) (3)	f_{25} (Jy) (4)	f_{60} (Jy) (5)	f_{100} (Jy) (6)	$\log L_{\mathrm{IR}}$ ($\log L_{\mathrm{IR}}/L_\odot$) (ergs s^{-1}) (7)	Far-infrared Color (8)
Arp 220	0.018	0.48	7.92	103.33	112.40	45.7 (12.1)	0.08 (cool)
Mrk 231	0.042	1.87	8.66	31.99	30.29	46.1 (12.5)	0.27 (warm)
IRAS 08572+3915	0.058	0.32	1.70	7.43	4.59	45.7 (12.1)	0.23 (warm)
VV 114 (IC 1623)	0.020	0.68	3.57	22.58	30.37	45.2 (11.6)	0.16 (cool)
He 2–10	0.003	1.09	6.51	24.08	26.40	43.5 (9.9) [a]	0.27 (warm)

Note. — Column (1): Object name. Column (2): Redshift. Columns (3)–(6): f_{12}, f_{25}, f_{60}, and f_{100} are *IRAS FSC* (or *PSC*) fluxes at 12, 25, 60, and 100 μm, respectively. Column (7): Decimal logarithm of the infrared (8–1000 μm) luminosity in ergs s^{-1} calculated as follows: $L_{\mathrm{IR}} = 2.1 \times 10^{39} \times$ D(Mpc)$^2 \times$ (13.48 $\times$ f_{12} + 5.16 $\times$ f_{25} + 2.58 $\times$ f_{60} + f_{100}) ergs s^{-1} (Sanders & Mirabel 1996). The values in parentheses are the decimal logarithms of the infrared luminosities in units of solar luminosities. Column (8): *IRAS* 25 μm to 60 μm flux ratio (f_{25}/f_{60}). LIRGs with f_{25}/f_{60} < (>) 0.2 are classified as cool (warm) (Sanders et al. 1988b).

[a]Distance of 10.5 Mpc (Tully 1988) is adopted.

Table 2.   Observing log

Object (1)	Array configuration (2)	Observing Date (UT) (3)	Central frequency (4)	Phase calibrator (5)	Band-pass calibrator (6)	Flux calibrator (7)
Arp 220	RAINBOW AB	2006 Jan 26, 28, 30 2007 Jan 22, 23, 24, 25	87.34	1538+149	3C 273	1741−038
Mrk 231	RAINBOW	2006 Jan 25, 26, 28	85.31	1418+546	3C 273	1741−038
IRAS 08572+3915	RAINBOW AB C D	2005 Jan 28 2006 Feb 12 2005 Mar 13, 14, 25, Dec 11, 13 2006 Mar 4, 5	84.04	0923+392	3C 84, 3C 273	3C 84
VV 114	AB C D	2007 Jan 29, 30, Feb 6, 7, 8 2007 Mar 29, 30 2006 Nov 28, 29, 30, Dec 1 2007 Apr 26, 27	87.16	0048−097	3C 84, 3C 454.3	Uranus
He 2–10	AB C D	2007 Feb 6 2007 Mar 28, 29, 30 2006 Dec 13, 2007 Apr 26, 27	88.64	0834−201	3C 84, 3C 279	3C 84

Note. — Column (1): Object name. Column (2): NMA array configuration. Column (3): Observing date in UT. Column (4): Central frequency used for the observations. Column (5): Object name used as a phase calibrator. Column (6): Object name used as a band-pass calibrator. Column (7): Object name used as a flux calibrator.

Table 3.   Parameters of final NMA/RAINBOW map

Object	On source integration (hr)	Beam size (arcsec × arcsec)	Position angle of the beam (°)
(1)	(2)	(3)	(4)
Arp 220	24	1.8 × 1.5	−55.1
Mrk 231	4	2.1 × 1.8	−34.8
IRAS 08572+3915	33	4.7 × 3.5	−50.7
VV 114	18	7.5 × 5.5	−13.2
He 2–10	13	10.8 × 5.5	−10.1

Note. — Col.(1): Object name. Col.(2): Net on-source integration time in hours. Col.(3): Beam size in arcsec × arcsec. Col.(4): Position angle of the beam pattern. It is 0° for the north-south direction, and increases counterclockwise on the sky plane.

Table 4.   Subaru IRCS observing log

Object	Date (UT)	Integration (Min)	Slit width (″)	P.A. (°)	Standard Stars Name	L-mag	Type	$T_{\rm eff}$ (K)
(1)	(2)	(3)	(4)	(5)	(6)	(7)	(8)	(9)
Arp 220	2006 July 17	24	0.6	87	HR 5728	4.5	G3V	5800
	2007 January 14	20	0.6	87	HR 5728	4.5	G3V	5800
Mrk 231	2007 January 14	16	0.6	90	HR 4767	4.8	F8-G0V	6000
IRAS 08572+3915NW	2007 January 15	24	0.9	90	HR 3451	5.0	F7V	6240
VV 114E	2006 July 19	24	0.6	60	HR 210	4.0	G3V	5800

Note. — Column (1): Object name. Col. (2): Observing date in UT. Col. (3): Net on-source integration time in min. Col. (4): Slit width in arcsec. Col. (5): Position angle of the slit. 0° corresponds to the north-south direction. Position angle increases counterclockwise on the sky plane. Col. (6): Standard star name. Col. (7): Adopted L-band magnitude. Col. (8): Stellar spectral type. Col. (9): Effective temperature.

Table 5.   Continuum emission

Object	Flux (mJy)	Frequency (GHz)
Arp 220	30	$\sim$87
Mrk 231	35	$\sim$85
IRAS 08572+3915NW	$<$3 ($<3\sigma$)	$\sim$84
VV 114	$<$4 ($<3\sigma$)	$\sim$87
He 2–10	$<$6 ($<3\sigma$)	$\sim$88.5

Table 6.   Gaussian fitting parameters of HCN(1–0) and HCO$^+$(1–0) emission lines

| Object | LSR velocity (km s^{-1}) | | | FWHM (km s^{-1}) | |
| | HCN(1–0) | HCO$^+$(1–0) | CO(1–0) or CO(2–1) | HCN(1–0) | HCO$^+$(1–0) |
(1)	(2)	(3)	(4)	(5)	(6)
Arp 220E	5640	5680	5650	240	190
Arp 220W	5310	5290	5340	320	270
Mrk 231	12660	12690	12650–12660	260	290
IRAS 08572+3915NW	17110 [a] + 17540 [a]	17250 [a] + 17900 [a]	17490	420 [a] + 300 [a]	320 [a] + 180 [a]
VV 114E-1	6090	$\cdots$	$\cdots$	170	$\cdots$
VV 114E-2	6070	6060	$\cdots$	190	260
VV 114-3	6060	6030	$\cdots$	290	360
VV 114-4	5910	5950	$\cdots$	250	310

Note. — Col.(1): Object name. Col.(2): LSR velocity $\{v_{opt} \equiv (\frac{\nu_0}{\nu} - 1) \times c\}$ of the HCN(1–0) emission peak. Col.(3): LSR velocity of the HCO$^+$(1–0) emission peak. Col.(4): LSR velocity of the CO(1–0) or CO(2–1) emission peak, taken from the literature (Bryant & Scoville 1996; Downes & Solomon 1998; Evans et al. 2002). Col.(5): Line width of the HCN(1–0) emission at FWHM. Col.(6): Line width of the HCO$^+$(1–0) emission at FWHM.

[a]A double Gaussian fit.

Table 7.   Flux of HCN(1–0), HCO$^+$(1–0), and CO(1–0) emission at each peak position

Nucleus	HCN(1–0) (Jy km s^{-1})	HCO$^+$(1–0) (Jy km s^{-1})	HCN(1–0)/HCO$^+$(1–0)	CO(1–0) (Jy km s^{-1})	Reference
(1)	(2)	(3)	(4)	(5)	(6)
Arp 220E	11.9	5.3	2.3	30 [a]	A
Arp 220W	17.8	6.6	2.7	47 [a]	A
Mrk 231	10.7	6.3	1.7	68	B
IRAS 08572+3915NW	2.3 (1.4 + 0.9) [b]	1.3 (0.7 + 0.6) [b]	1.8	11.8	C
VV 114E-1	2.7	<1.7	>1.6	<70 [c]	D
VV 114E-2	1.9	4.0	0.5	· · ·	· · ·
VV 114-3	3.2	5.5	0.6	· · ·	· · ·
VV 114-4	1.3	6.0	0.2	· · ·	· · ·
He 2–10	6.1 [d]	11 [d]	<0.6 [e]	30	E

Note. — Col.(1): Object name. Col.(2): Integrated HCN(1–0) intensity at an emission peak. Col.(3): Integrated HCO$^+$(1–0) intensity at an emission peak. Col.(4): HCN(1–0)/HCO$^+$(1–0) ratio in brightness temperature ($\propto \lambda^2 \times$ flux density) at an emission peak. The ratio is not affected by possible absolute flux uncertainties in the NMA/RAINBOW data (see §5.1). Col.(5): Integrated CO(1–0) intensity at an emission peak taken from the literature. Col.(6): References for interferometric CO(1–0) flux measurements. (A): Sakamoto et al. (1999). (B): Downes & Solomon (1998). (C): Evans et al. (2002) (D): Iono et al. (2004). (E): Kobulnicky et al. (1995).

[a]CO(2–1) emission is detected at individual cores, but CO(1–0) emission is not (Downes & Solomon 1998). We estimate the CO(1–0) flux *at the core* from the CO(2–1) flux (Sakamoto et al. 1999), using the ν^2 scaling (Riechers et al. 2006), based on the assumption that emission is thermalized and that both CO(1–0) and CO(2–1) have the same brightness temperatures.

[b]Blue (former) and red (latter) components from the double Gaussian fits (see §4.1).

[c]CO(1–0) flux is estimated from CO(3–2) flux, by assuming the ν^2 scaling.

[d]Flux is derived from the peak contour of the integrated intensity map. Possible continuum emission is not subtracted, because it is difficult to estimate in a reliable way due to the large scatter of the spectrum.

[e]The ratio is an upper limit because possible continuum emission is not subtracted and HCN(1–0) emission is weaker than HCO$^+$(1–0) emission.

Table 8.   Total flux of HCN(1–0) and HCO$^+$(1–0) emission for sources that show spatially-extended components

Nucleus	HCN(1–0) (Jy km s^{-1})	HCO$^+$(1–0) (Jy km s^{-1})
(1)	(2)	(3)
Arp 220	34	18
VV 114	7	19
He 2–10	6.5	11

Note. — Col.(1): Object name. Col.(2): Total HCN(1–0) flux. Col.(3): Total HCO$^+$(1–0) flux.

Table 9.   Comparison of HCN(1–0) and HCO$^+$(1–0) fluxes between our measurements and those in the literature

Nucleus (1)	Line (2)	Flux (3)	Reference (4)
Arp 220	HCN(1–0)	34[a]	This work
		45	Evans et al. (2006)
		37	Solomon et al. (1992)
		35[a]	Radford et al. (1991)
	HCO$^+$(1–0)	18[a]	This work
		23	Gracia-Carpio et al. (2006)
Mrk 231	HCN(1–0)	11[a]	This work
		14	Solomon et al. (1992)
	HCO$^+$(1–0)	6[a]	This work
		8	Gracia-Carpio et al. (2006)

Note. — Col.(1): Object name. Col.(2): HCN(1–0) or HCO$^+$(1–0) line. Col.(3): Flux in [Jy km s^{-1}]. Col.(4): Reference.

[a]Measurements are made based on interferometric data.

Table 10.   Strength of the 3.3 μm PAH emission feature

Object (1)	$f_{3.3PAH}$ ($\times 10^{-14}$ ergs s^{-1} cm^{-2}) (2)	$L_{3.3PAH}$ ($\times 10^{40}$ ergs s^{-1}) (3)	$L_{3.3PAH}/L_{IR}$ ($\times 10^{-3}$) (4)	rest EW$_{3.3PAH}$ (nm) (5)
Arp 220E	3.5	2.2	$\cdots$	85
Arp 220W	7.5	4.8	$\cdots$	95
Arp 220E+W	11.0	6.9	0.01	95
Mrk 231	9.5	33.5	0.03	1.5
IRAS 08572+3915NW	<4.0	<30.0	<0.05	<3
VV 114E	3.0	2.5	$\cdots$	20
VV 114E$_{SW}$	2.5	2.0	$\cdots$	110

Note. — Col.(1): Object name. Col.(2): Observed flux of the 3.3 μm PAH emission. Col.(3): Observed luminosity of the 3.3 μm PAH emission. Col.(4): Observed 3.3 μm PAH-to-infrared luminosity ratio in units of 10^{-3}, a typical value for a modestly-obscured (A$_V$ < 15 mag) normal starburst (Mouri et al. 1990; Imanishi 2002). For Arp 220E, W and VV 114E, E$_{SW}$, no values are shown, because the fraction of *IRAS*-measured infrared fluxes, coming from individual nuclei, is unknown. Col.(5): Rest-frame equivalent width of the 3.3 μm PAH emission. Normal starbursts have EW$_{3.3PAH}$ ∼ 100 nm (Imanishi & Dudley 2000).
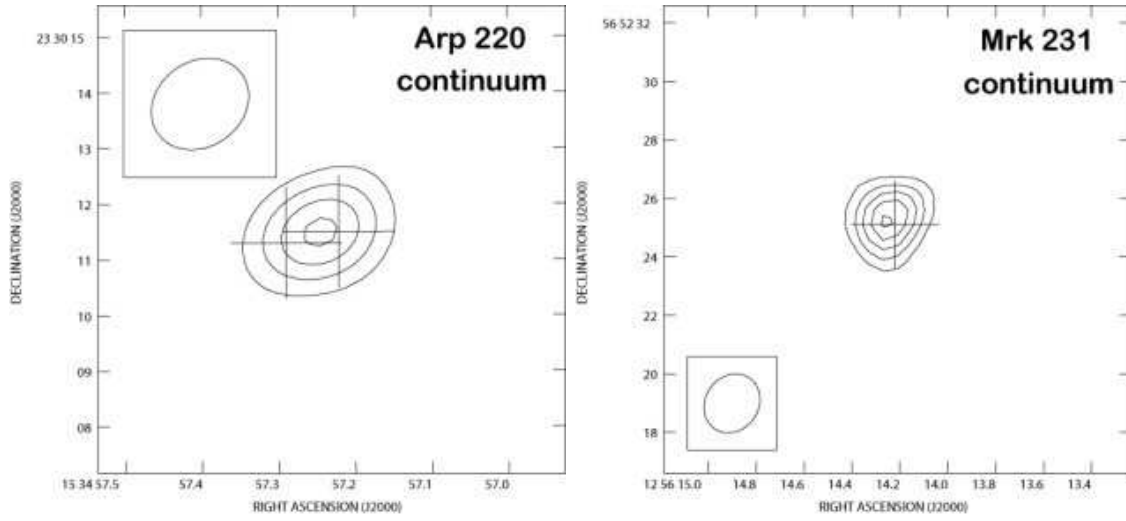
Fig. 1.— Continuum maps of Arp 220 at $\sim$87 GHz and Mrk 231 at $\sim$85 GHz. The crosses show the coordinates of main nuclei. The coordinates in J2000 are ($15^h34^m57.22^s$, $+23°30'11\overset{''}{.}5$) for Arp 220W, ($15^h34^m57.29^s$, $+23°30'11\overset{''}{.}3$) for Arp 220E, and ($12^h56^m14.22^s$, $+56°52'25\overset{''}{.}1$) for Mrk 231. These nuclear coordinates are adopted from CO(2–1) peaks in millimeter interferometric maps (Downes & Solomon 1998). The contours are $3 \times$ (3, 5, 7, 9) mJy beam^{-1} for Arp 220, $3 \times$ (3, 5, 7, 9, 11) mJy beam^{-1} for Mrk 231.
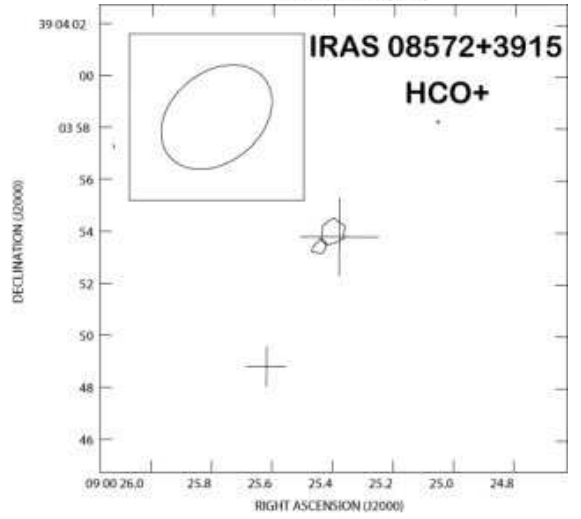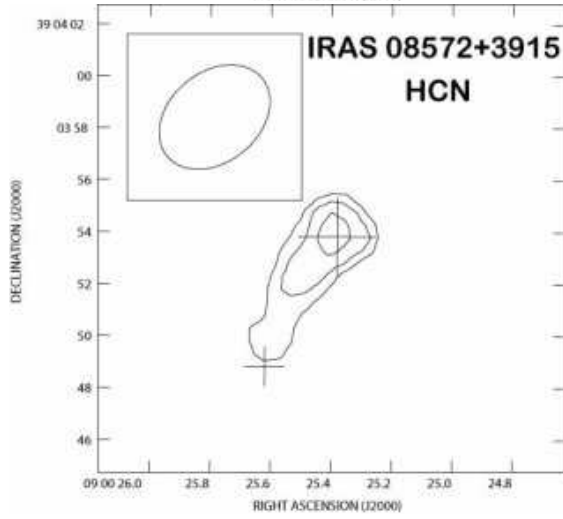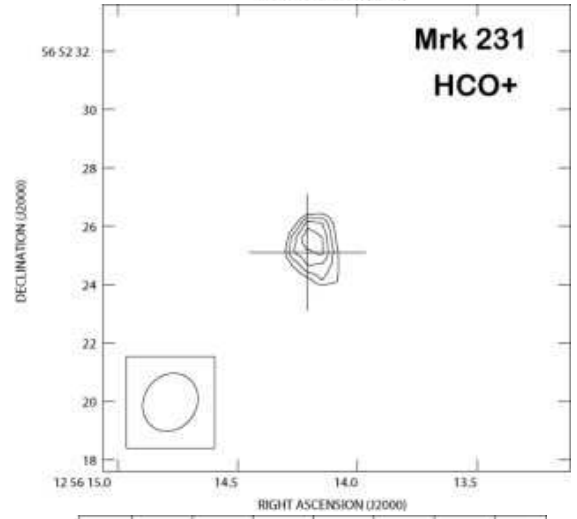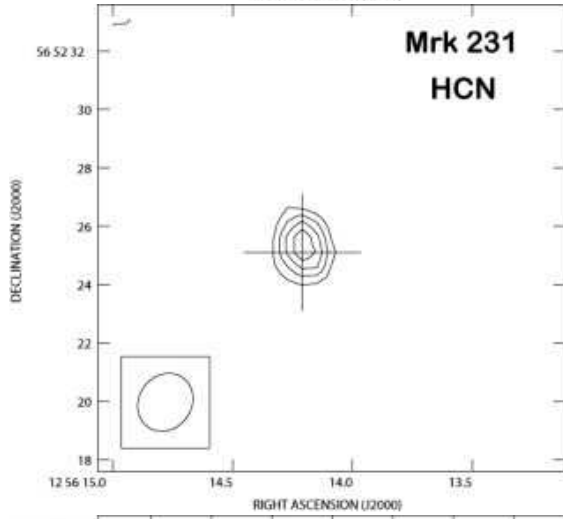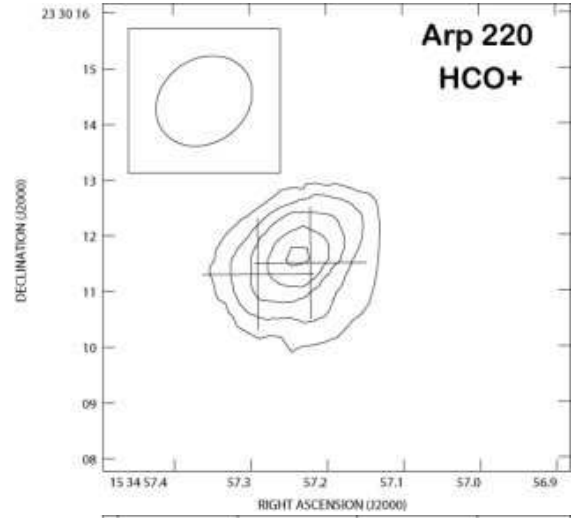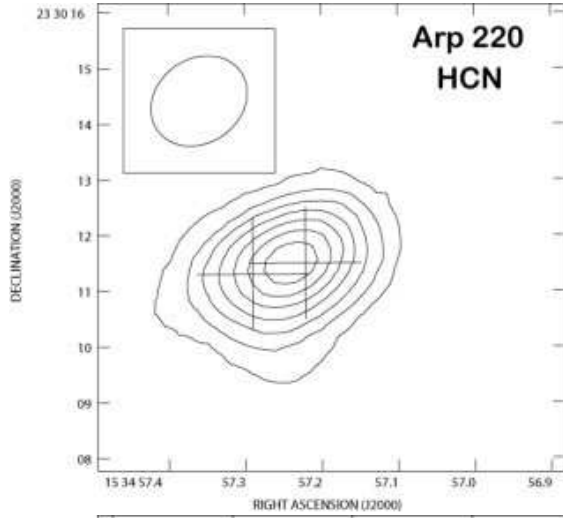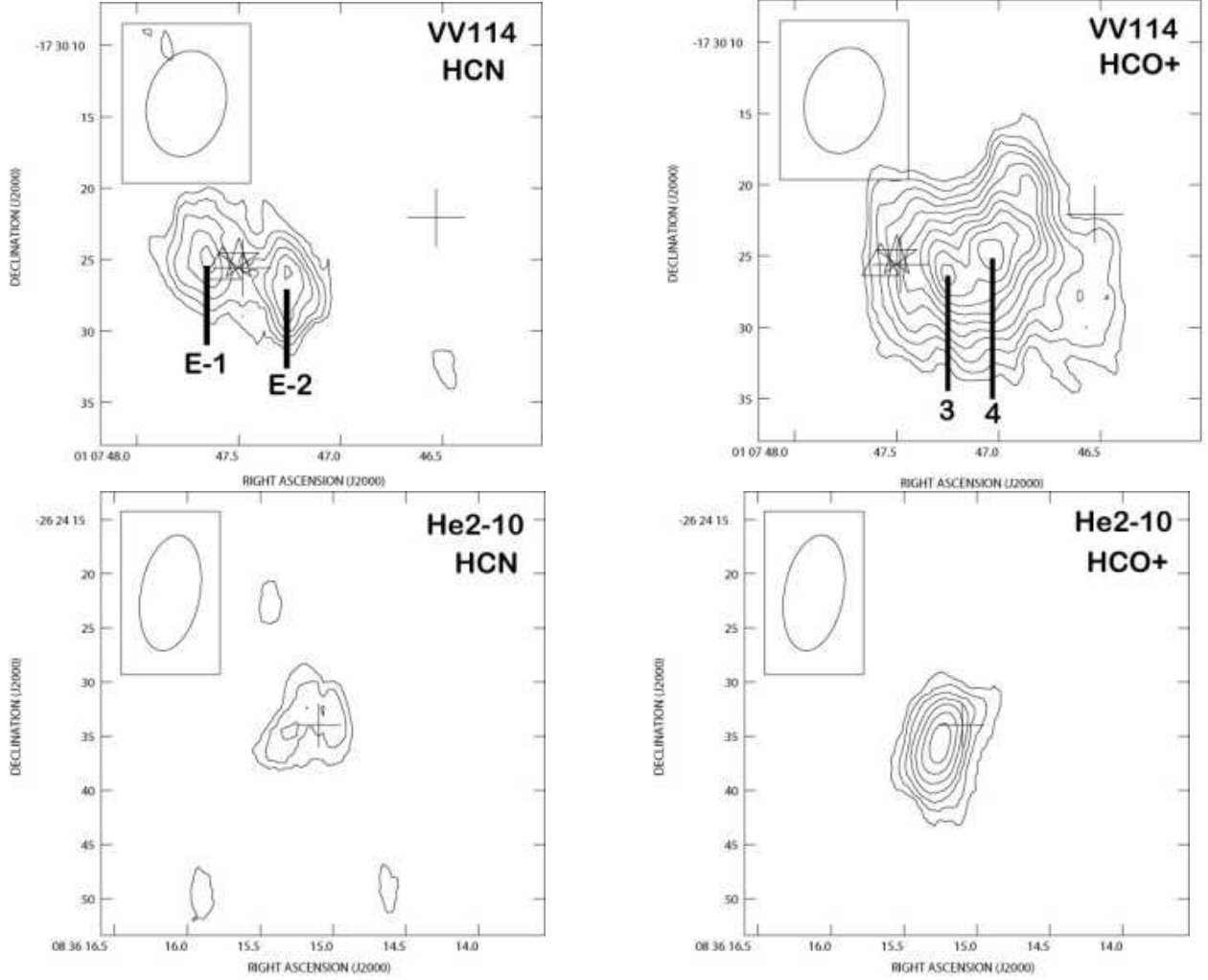
Fig. 2.— *Left*: HCN(1–0) emission map. The contours are $0.85 \times$ (3, 7, 11, 15, 19, 23, 27) Jy km s^{-1} beam^{-1} for Arp 220, $0.76 \times$ (4, 6, 8, 10) Jy km s^{-1} beam^{-1} for Mrk 231, $0.6 \times$ (3, 4, 5) Jy km s^{-1} beam^{-1} for IRAS 08572+3915, $0.5 \times$ (3, 4, 5, 6, 7, 8) Jy km s^{-1} beam^{-1} for VV 114, and $1.2 \times$ (3, 4, 5) Jy km s^{-1} beam^{-1} for He 2–10. For IRAS 08572+3915, the two crosses correspond to the NW ($9^h0^m25.38^s$, $+39°3'53\overset{''}{.}8$) and SE ($9^h0^m25.62^s$, $+39°3'48\overset{''}{.}8$) peaks in J2000 (Evans et al. 2002). For VV 114, the two crosses are near-infrared peaks, VV 114E ($1^h7^m47.48^s$, $-17°30'25\overset{''}{.}6$) and VV 114W ($1^h7^m46.53^s$, $-17°30'22\overset{''}{.}1$) in J2000, whose coordinates are converted from B1950 (Knop et al. 1994), using NED. The open star is CO(3–2) peak ($1^h7^m47.5^s$, $-17°30'25\overset{''}{.}0$) in J2000 (Iono et al. 2004), and the open triangle is a radio 3.55 cm (8.44 GHz) peak ($1^h7^m47.58^s$, $-17°30'25\overset{''}{.}6$) in J2000, converted from B1950 (Condon et al. 1991) using NED. E-1 and E-2 correspond to the two emission peaks in the HCN(1–0) map. For He 2–10, the cross is CO (1–0) peak ($8^h36^m15.1^s$, $-26°24'34\overset{''}{.}0$) in J2000, converted from B1950 (Kobulnicky et al. 1995) using NED. *Right*: HCO$^+$(1–0) emission map. The contours are $0.85 \times$ (3, 5, 7, 9, 11) Jy km s^{-1} beam^{-1} for Arp 220, $0.76 \times$ (3, 4, 5, 6) Jy km s^{-1} beam^{-1} for Mrk 231, 0.6×3 Jy km s^{-1} beam^{-1} for IRAS 08572+3915, $0.5 \times$ (3, 4, 5, 6, 7, 8, 9, 10, 11, 12) Jy km s^{-1} beam^{-1} for VV 114, and $1.2 \times$ (3, 4, 5, 6, 7, 8, 9) Jy km s^{-1} beam^{-1} for He 2–10. For VV 114, the positions 3 and 4 correspond to the two emission peaks in the HCO$^+$(1–0) map. For IRAS 08572+3915 and He 2–10, possible continuum emission is not subtracted from both the HCN(1–0) and HCO$^+$(1–0) maps (see §4.1).
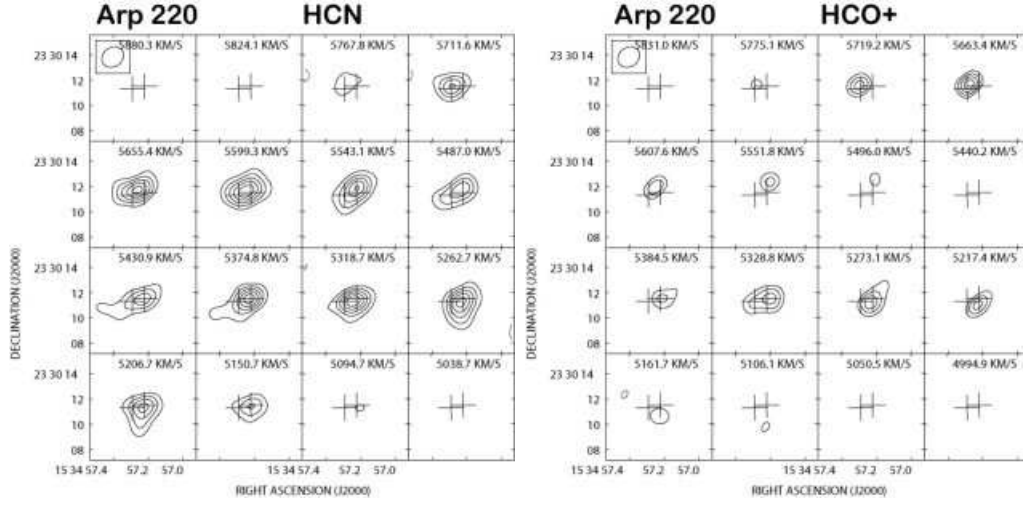
Fig. 3.— Channel maps of HCN(1–0) and HCO$^+$(1–0) emission for Arp 220. *Left*: HCN(1–0) emission. The contours are $4 \times (-3, 3, 5, 7, 9, 11)$ mJy beam^{-1}. The r.m.s. noise level is $\sim$4 mJy beam^{-1}. *Right*: HCO$^+$(1–0) emission. The contours are $4 \times (-3, 3, 4, 5, 6)$ mJy beam^{-1}. The r.m.s. noise level is $\sim$4 mJy beam^{-1}.
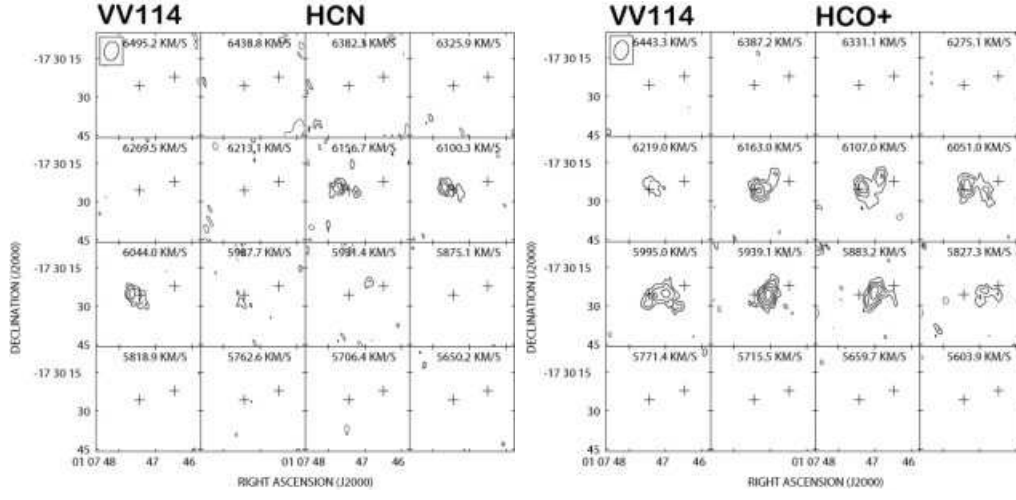
Fig. 4.— Channel maps of HCN(1–0) and HCO$^+$(1–0) emission for VV 114. *Left*: HCN(1–0) emission. The contours are $3 \times (-3, 3, 4, 5)$ mJy beam^{-1}. The r.m.s. noise level is $\sim$3 mJy beam^{-1}. *Right*: HCO$^+$(1–0) emission. The contours are $3 \times (-3, 3, 4, 5, 6, 7)$ mJy beam^{-1}. The r.m.s. noise level is $\sim$3 mJy beam^{-1}.
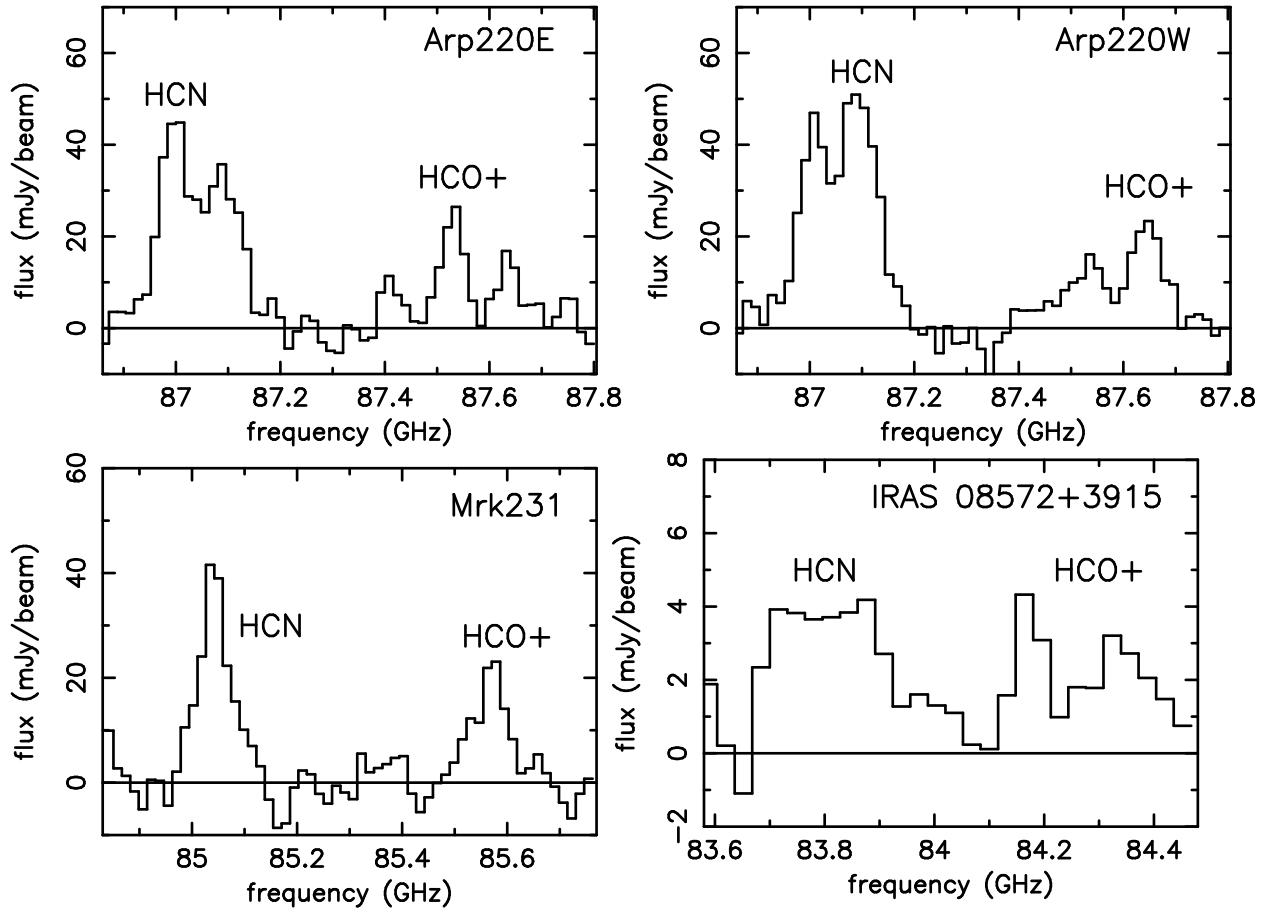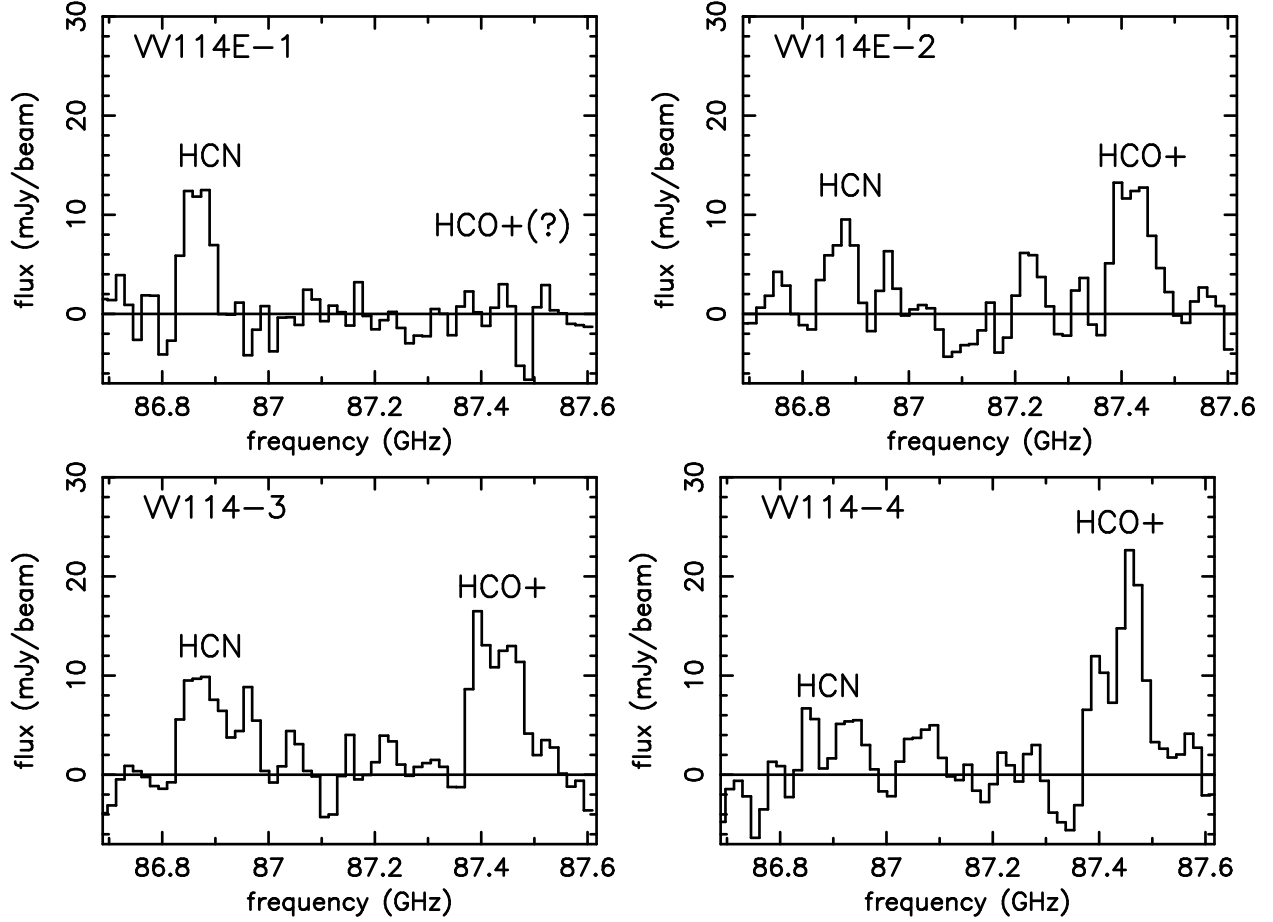
Fig. 5.— HCN(1–0) and HCO$^+$(1–0) spectra of the observed LIRGs. The abscissa is the observed frequency in GHz and the ordinate is flux in mJy beam^{-1}. For Arp 220 and Mrk 231, the strong continuum emission is subtracted. For VV 114, a possible continuum is subtracted. For IRAS 08572+3915, the continuum is not subtracted, because its subtraction introduces a significant uncertainty, given the faintness of the HCN(1–0) and HCO$^+$(1–0) emission lines. Appropriate spectral binning is made, depending on the signal levels of the HCN(1–0) and HCO$^+$(1–0) emission lines. The r.m.s. noise levels per spectral bin in the final spectra are ∼4 mJy (Arp 220), ∼6 mJy (Mrk 231), ∼1.5 mJy (IRAS 08572+3915), and ∼3 mJy (VV 114).

– 35 –
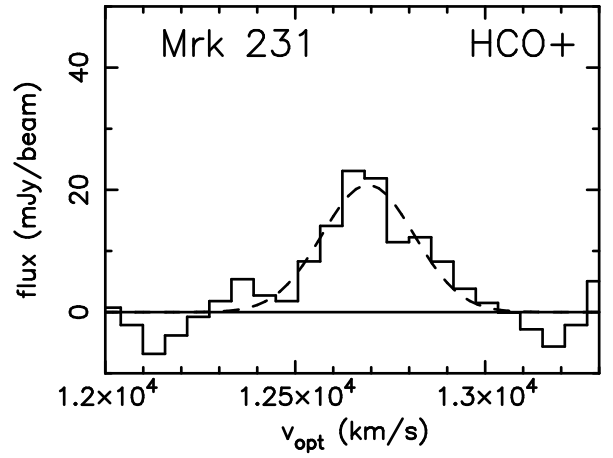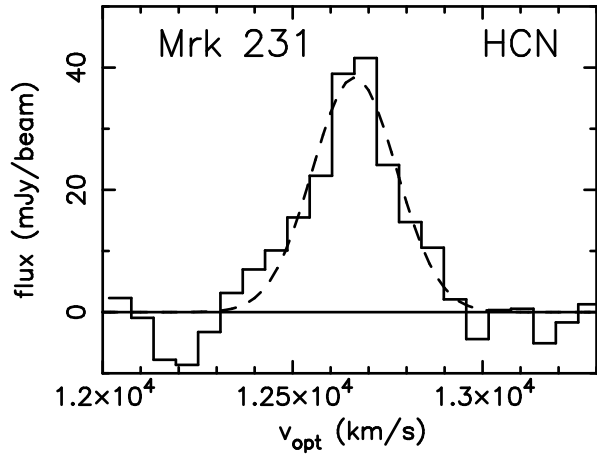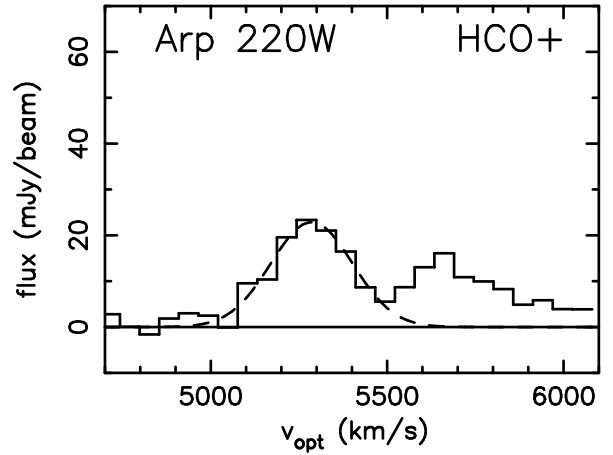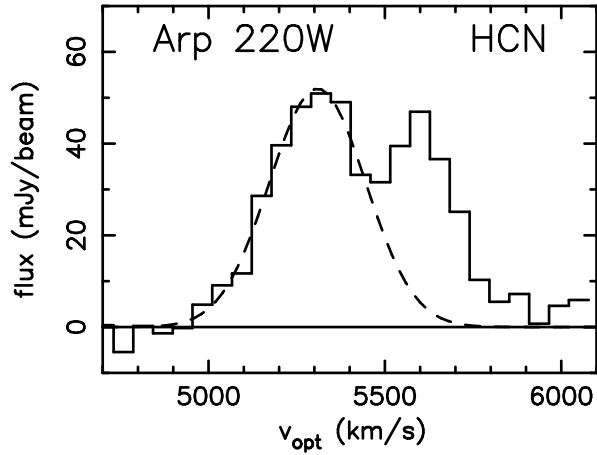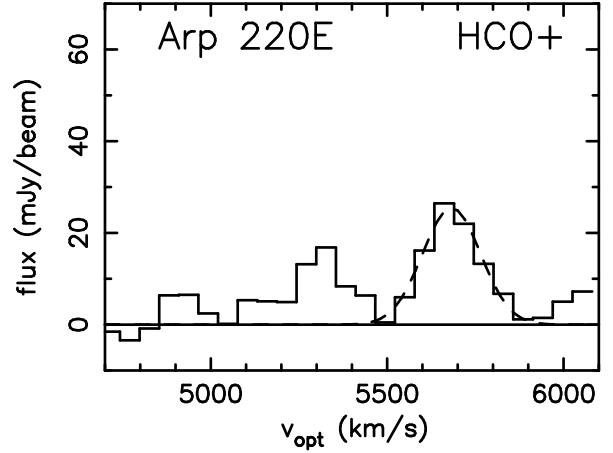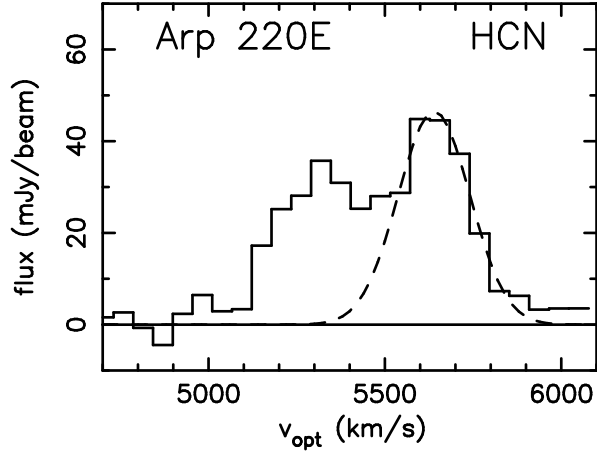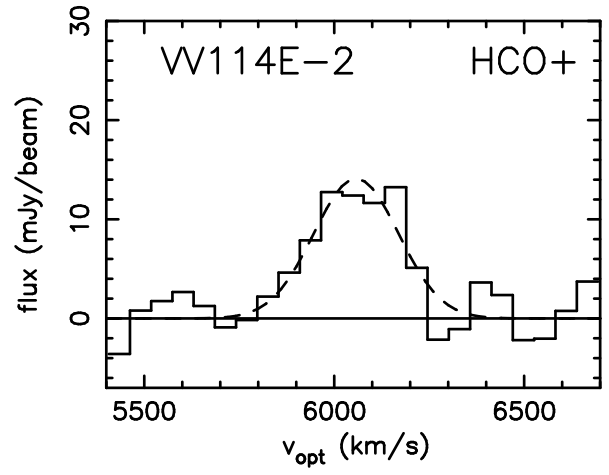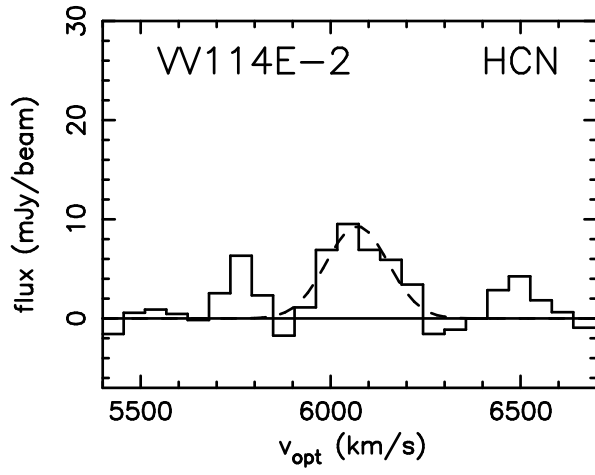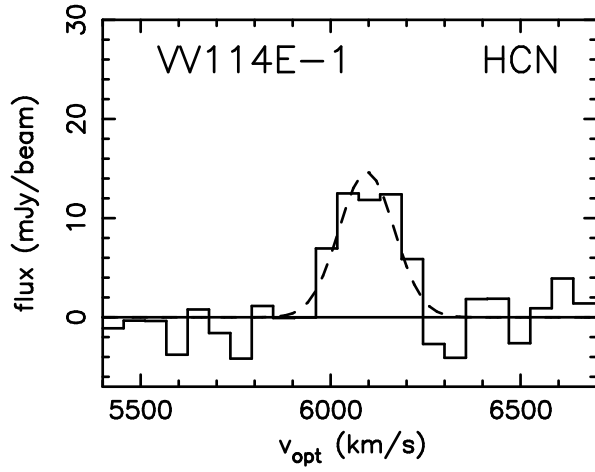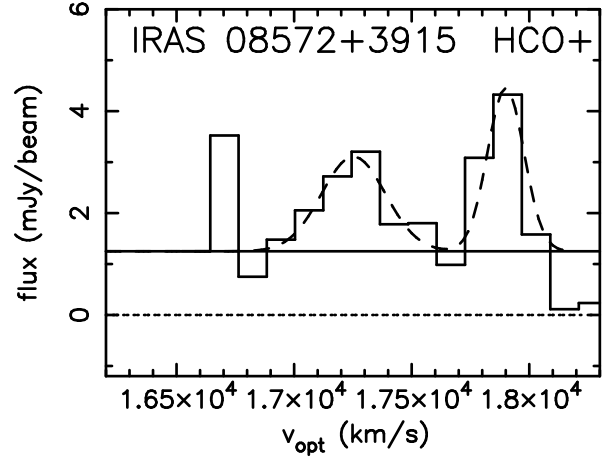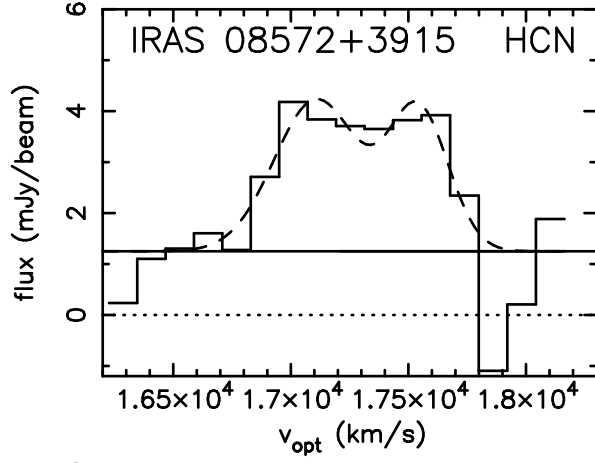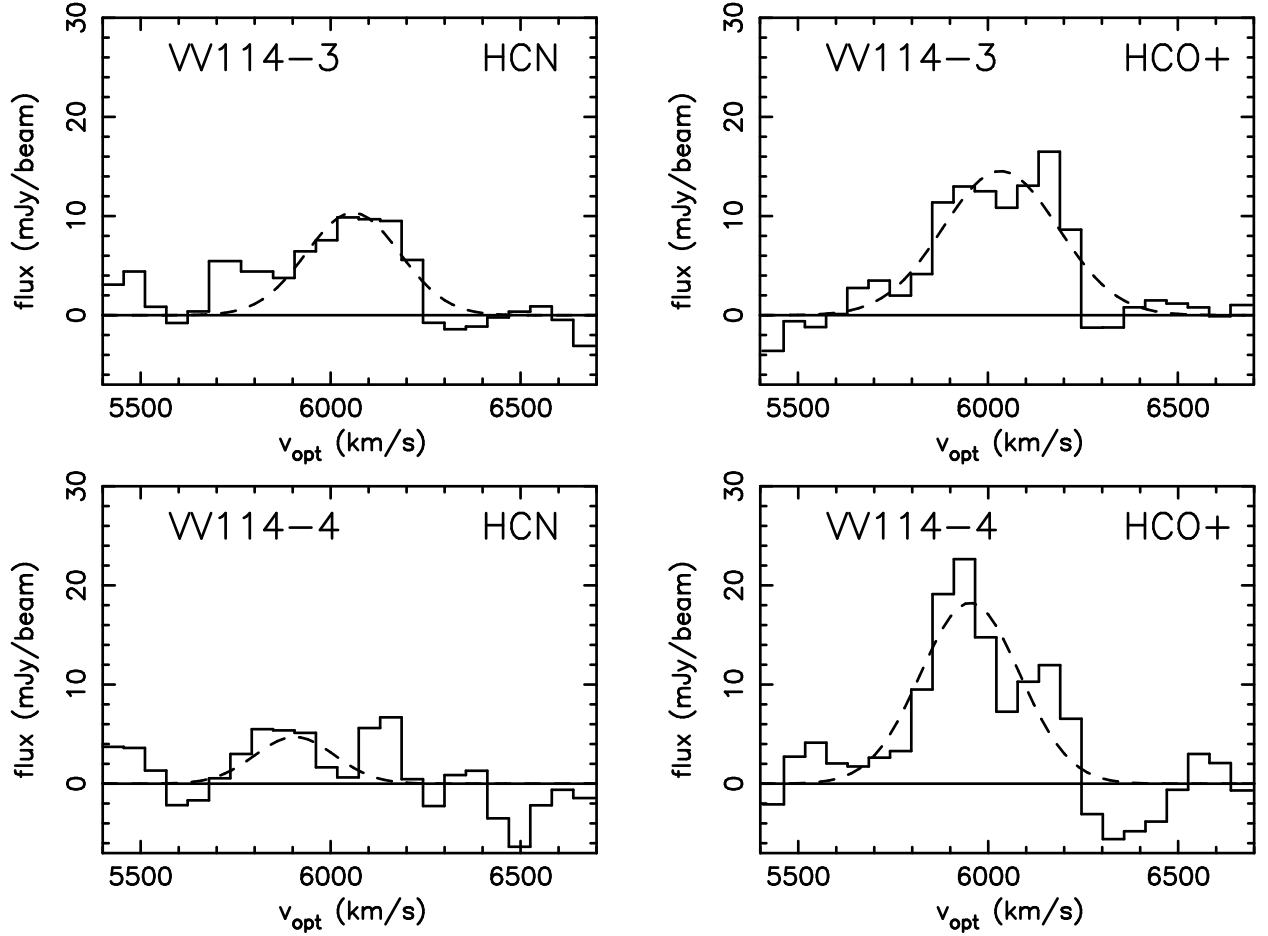
Fig. 6.— Gaussian fits to the detected HCN(1–0) and HCO$^+$(1–0) emission lines. The abscissa is the LSR velocity $\{v_{opt} \equiv (\frac{\nu_0}{\nu} - 1) \times c\}$ in km s^{-1} and the ordinate is flux in mJy beam^{-1}. Single Gaussian fits are used as defaults and are shown as dashed lines. The spectrum of IRAS 08572+3915 is only for the NW nucleus. For this source, since evidence for double peaks exists, we attempted a double Gaussian fit, shown as dashed lines. A constant continuum is assumed and is set as a free parameter because the continuum emission was not subtracted from the spectrum of IRAS 08572+3915. For other sources, the continuum level is set as the zero value. The adopted continuum levels are shown as the horizontal solid straight lines for all sources.
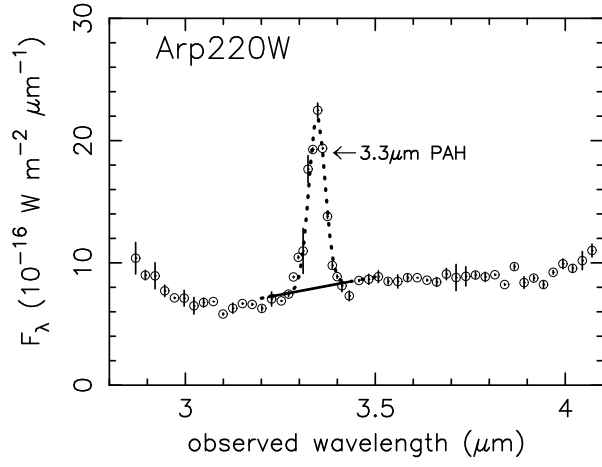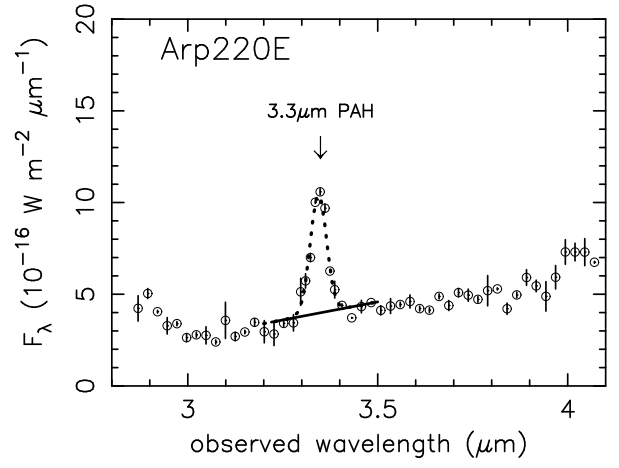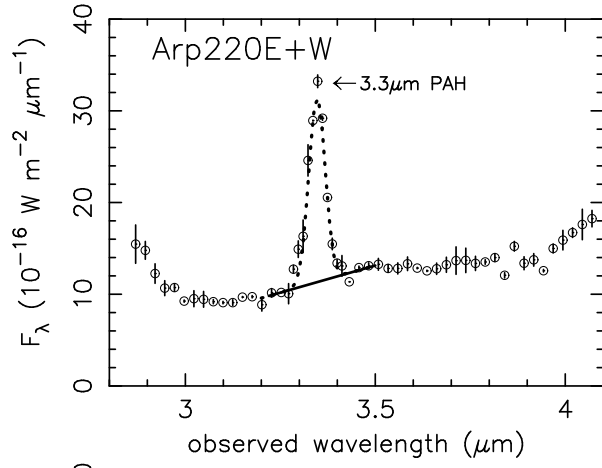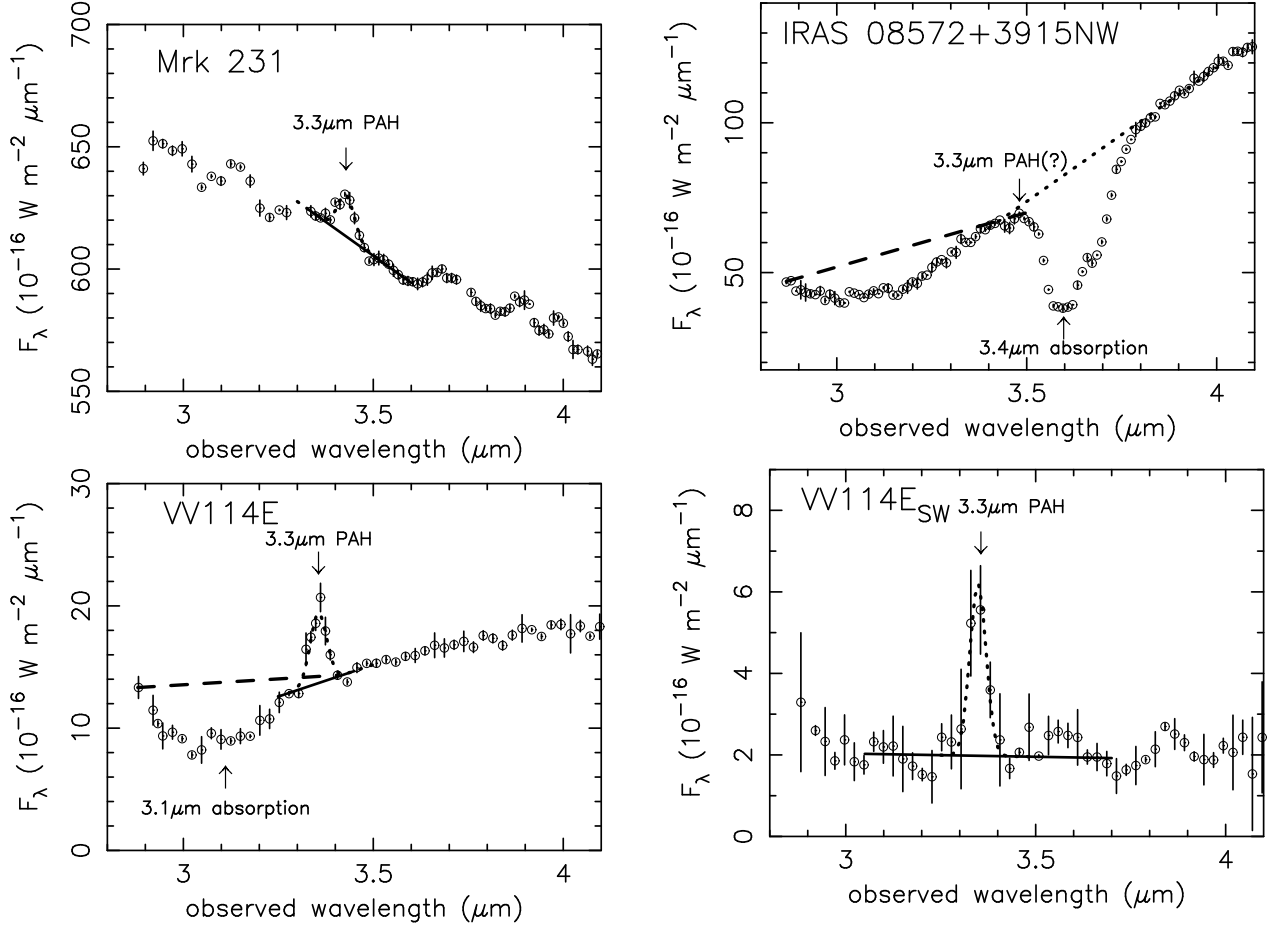
Fig. 7.— Newly obtained infrared 2.8–4.1 μm (L-band) spectra of Arp 220, Mrk 231, IRAS 08572+3915NW, and VV 114. The abscissa is observed wavelength in μm, and the ordinate is F_λ in 10^{-16} W m^{-2} μm^{-1}. Dashed straight line: Adopted continuum level to measure the optical depth of the 3.1 μm ice absorption feature. Dotted line: Gaussian fit to the 3.3 μm PAH emission feature. Solid straight line: Adopted continuum level to measure the strength of the 3.3 μm PAH emission feature. Dotted straight line for IRAS 08572+3915 is the adopted continuum level to measure the optical depth of the 3.4 μm carbonaceous dust absorption feature.
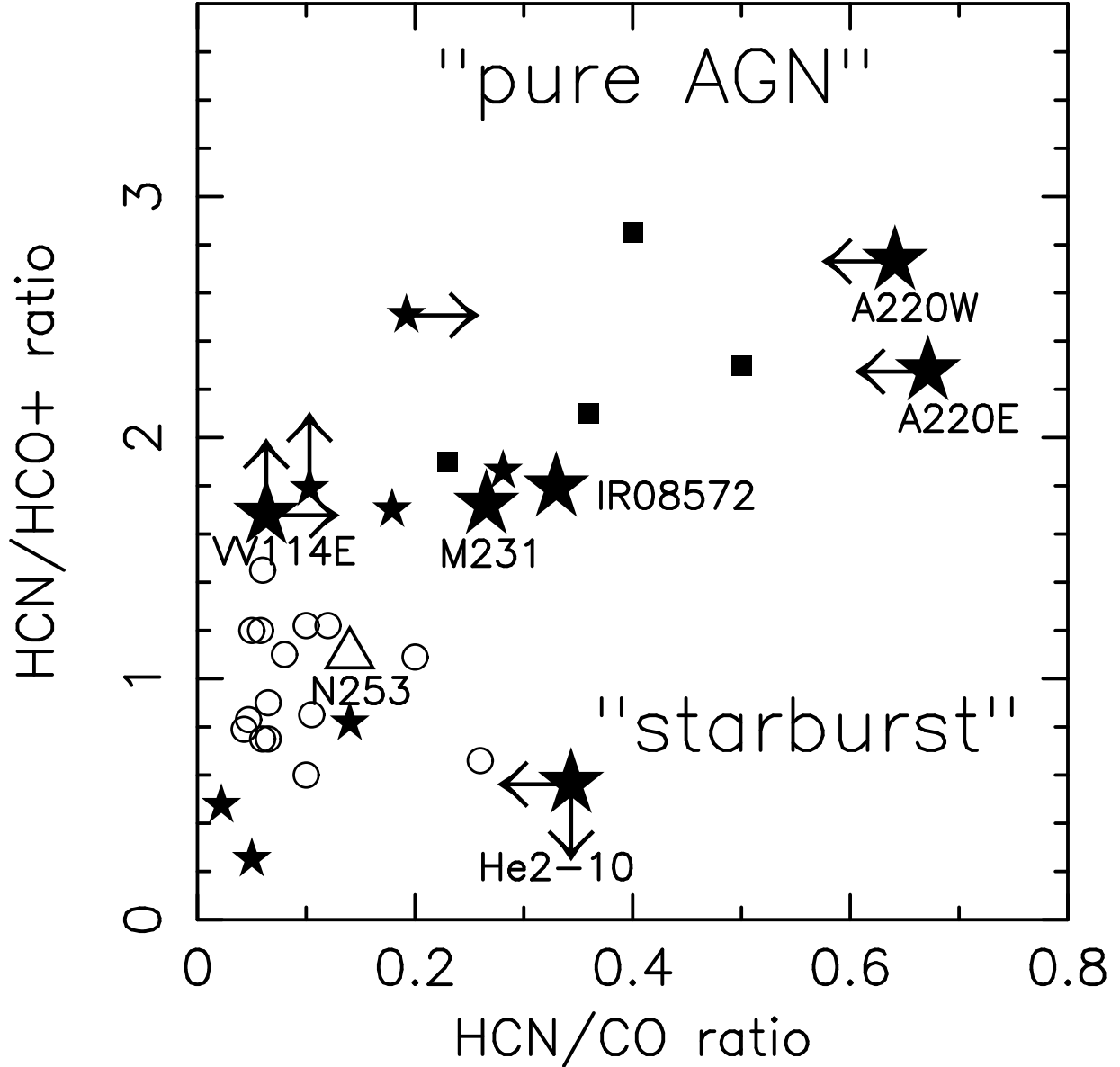
Fig. 8.— HCN(1–0)/HCO$^+$(1–0) (ordinate) and HCN(1–0)/CO(1–0) (abscissa) ratios in bright-ness temperature ($\propto \lambda^2 \times$ flux density), derived from our NMA/RAINBOW interferometric ob-servations. Arp 220, Mrk 231, IRAS 08572+3915, VV 114, and He 2–10 are plotted as large filled stars with labels. Other LIRGs previously observed by Imanishi et al. (2004, 2006b) and Imanishi & Nakanishi (2006) are also plotted as small filled stars. Other data points are taken from Kohno (2005), where sources with AGN-like (starburst-like) ratios are marked with filled squares (open circles). The ratio at the core of the starburst galaxy NGC 253, derived by spatially-resolved interferometric data (Knudsen et al. 2007), is also plotted as a large open triangle. For LIRGs and He 2–10, the HCN(1–0)/HCO$^+$(1–0) brightness-temperature ratios are derived directly from our interferometric data, while the HCN(1–0)/CO(1–0) ratios are derived by combining our data with CO data in the literature. The HCN(1–0)/CO(1–0) ratio in Arp 220 is taken as an upper limit, because the beam size of CO observations is much smaller. For all LIRGs' nuclei, the HCN(1–0)/HCO$^+$(1–0) brightness-temperature ratios in the ordinate are those toward the cores, where putative buried AGNs are expected to reside in. Contamination from extended starburst emission outside the beam sizes (Table 3) are totally removed.
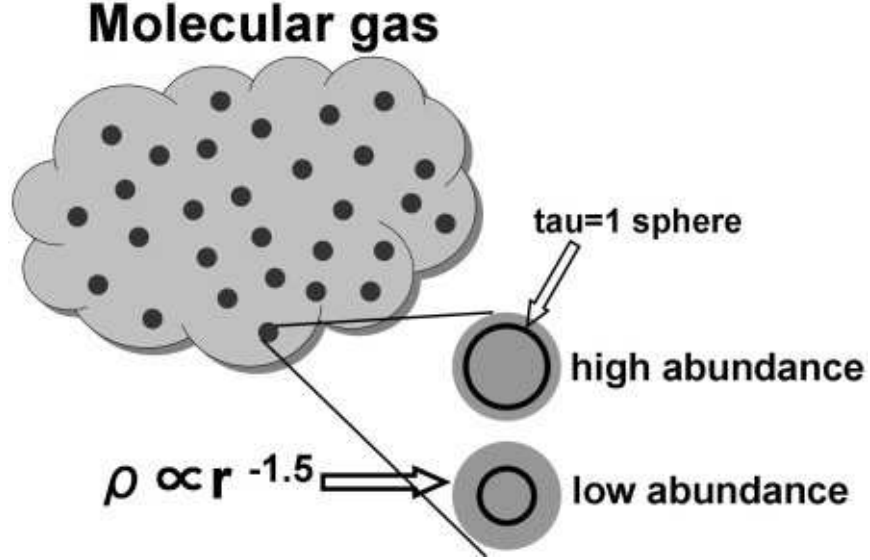
Fig. 9.— Schematic diagram of molecular gas in the current standard model (Solomon et al. 1987). Molecular gas consists of dense clumps (shown as dark filled circles in the upper-left panel) with a small volume filling factor. HCN(1–0) and HCO$^+$(1–0) lines can be moderately optically thick for each clump (Nguyen-Q-Rieu et al. 1992). It is very likely that each clump has a decreasing radial density profile ($\propto r^\alpha$; $\alpha < 0$). If the radial density distribution of $r^{-1.5}$ is assumed (Gierens et al. 1992), line emission comes mainly from the layer where an optical depth reaches about unity ($\tau \sim 1$) (Gierens et al. 1992). When a molecular abundance increases (decreases), the $\tau \sim 1$ layer for certain molecular line moves outward (inward). Consequently, the surface area of the layer, or its area filling factor in molecular gas, becomes larger (smaller), increasing (decreasing) the flux of that molecular line.
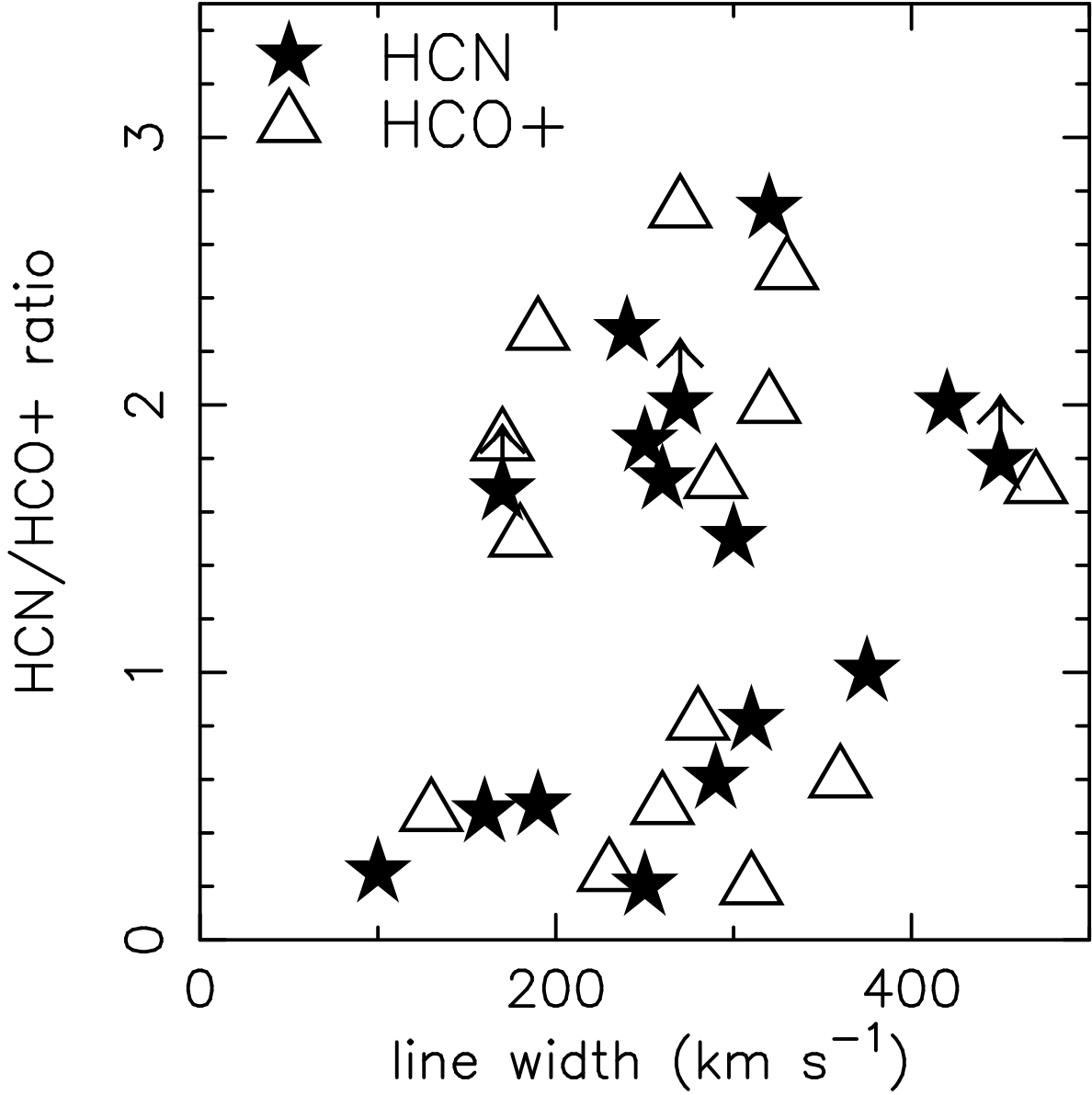
Fig. 10.— Comparison between FWHM line widths of molecular lines (abscissa) and HCN(1–0)/HCO$^+$(1–0) brightness-temperature ratio (ordinate). Filled stars: HCN(1–0) line width. Open triangles: HCO$^+$(1–0) line width. All LIRGs with available NMA/RAINBOW HCN(1–0) and HCO$^+$(1–0) data are plotted. These LIRGs are NGC 4418 (Imanishi et al. 2004), UGC 5101, Mrk 273, IRAS 17208−0014 (Imanishi et al. 2006b), Arp 299 A, B, C (Imanishi & Nakanishi 2006), and the four LIRGs (This paper). The HCN(1–0) line width of UGC 5101, and the HCN(1–0) and HCO$^+$(1–0) line widths of IRAS 08572+3915 are for individual components of the double Gaussian fits (Imanishi et al. 2006b; This paper). The HCN(1–0)/HCO$^+$(1–0) brightness-temperature ratios are also derived for individual components of the double Gaussian fits (Imanishi et al. 2006b; This paper). For Mrk 273 and VV 114E-1, no HCO$^+$(1–0) line width information is available (Imanishi et al. 2006b; This paper). The FWHM line widths of NGC 4418 are 250 km s^{-1} [HCN(1–0)] and 170 km s^{-1} [HCO$^+$(1–0)], which are estimated from the data of Imanishi et al. (2004).
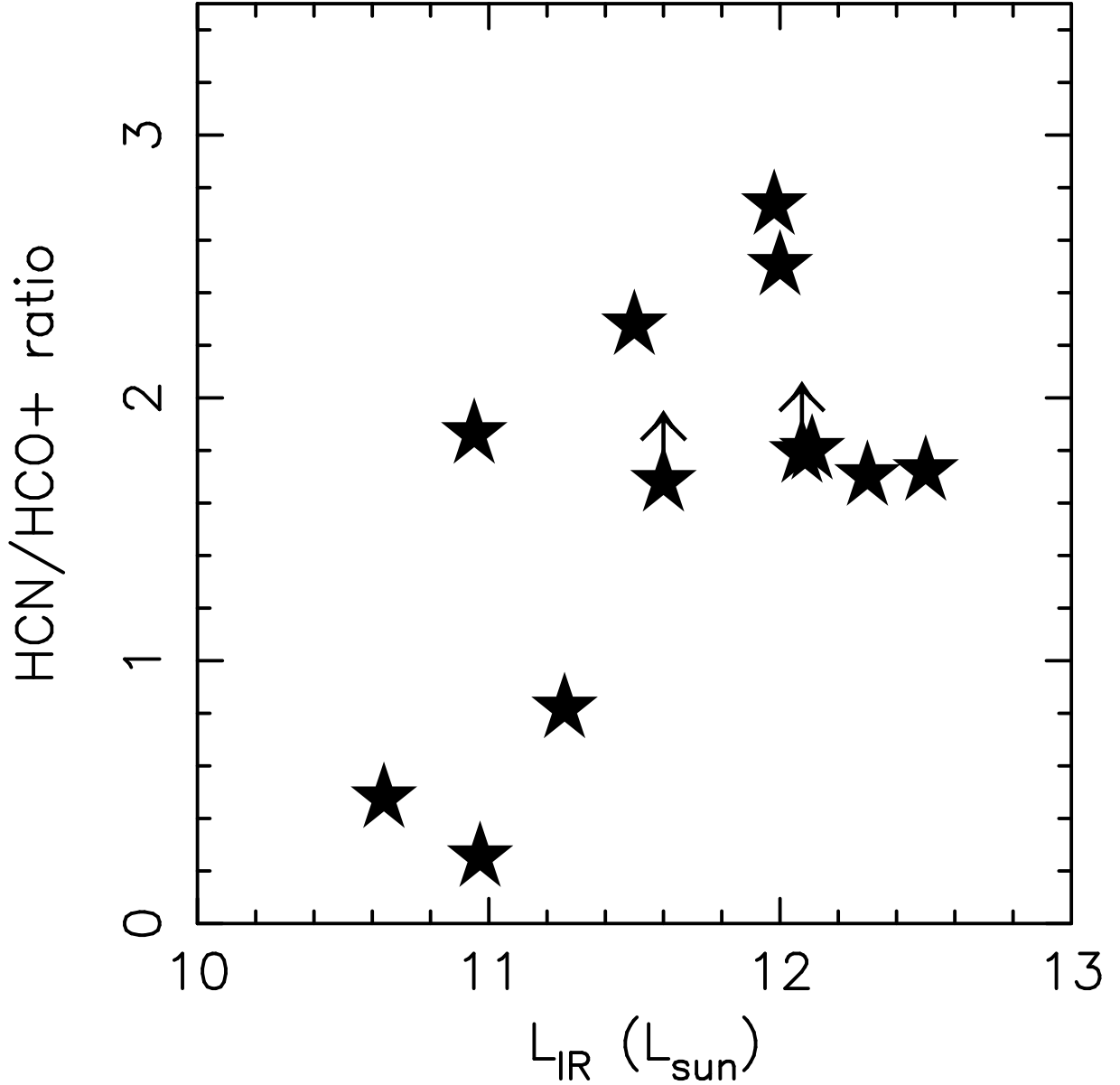
Fig. 11.— Comparison between *IRAS*-measured infrared luminosity in units of the solar luminosity (abscissa) and HCN(1–0)/HCO$^+$(1–0) brightness-temperature ratio (ordinate). The HCN(1–0)/HCO$^+$(1–0) ratio in the ordinate is only for the core emission within the beam size of interferometric maps, while the infrared luminosity in the abscissa traces the emission from the whole galaxy regions. For VV 114, we plot the HCN(1–0)/HCO$^+$(1–0) brightness-temperature ratio at VV 114E-1, and assume that the infrared luminosity of VV 114 is dominated by VV 114E. For UGC 5101 and IRAS 08572+3915, the HCN(1–0)/HCO$^+$(1–0) brightness-temperature ratios are derived by summing the both components of the double Gaussian fits. For Arp 220, we assume that Arp 220 W and E have, respectively, 75% and 25% of the total infrared luminosity (Downes & Eckart 2007). For Arp 299, the infrared luminosities of Arp 299 A, B, C are taken from Charmandaris et al. (2002).